PROPAGATION PATH DISTORTION OF LIGHTNING PRODUCED TRANSIENT WAVEFORMS

Lightning Phenomenology Notes

Note 7

Robert L. Gardner
Mission Research Corporation

ABSTRACT

In this note we describe and exercise a detailed model of the lightning return stroke and calculate the radio frequency electromagnetic fields emitted from the lightning stroke. The model uses a tortuous channel constructed of straight line segments on which a specified current waveform propagates at a known, arbitrary velocity. Once the current is established on the channel the electromagnetic fields as a function of distance and frequency are computed. Effects of an imperfectly conducting earth and an anisotropic ionosphere are calculated.

Finally, a signal function is introduced to separate some of the bulk characteristics of the stroke, such as overall length from the field spectra.

CONTENTS

ILLUSTRATIONS

ILLUSTRATIONS (Concluded)

INTRODUCTION

The lightning return stroke radiates radio frequency electromagnetic fields that may be measured and used to study the properties of the return stroke current. Measured fields are usually in the form of transient waveforms. Lightning discharges occur at uncontrolled distances from the observer and the surrounding earth and ionosphere tend to distort the waveforms. This distortion must be removed prior to comparing the electromagnetic signals from two lightning strokes. Waveforms at varying distances but with colinear observation points are required to quantify the wave distortion for a given path. When verified, theoretical models may then be used to correct lightning data for propagation path distortion so that correct inferences about the discharge current may be made.

Lightning propagation models currently used in the lightning literature have assumed a perfectly conducting ground. Complications in the models have generally been made in the description of the source current and source geometry rather than in the propagation path model (Ref. 1).

In several papers (Refs. 2 through 4), M. A. Uman and his colleagues have developed a model of the return stroke fields using a line source and a perfectly conducting earth. A current waveform propagates up the channel without change of shape in the vertical direction at a velocity v.

Reference 5 presents an exact solution to Maxwell's equations for a very idealized vertical source. The major restriction in their solution is that the current pulse must propagate along the channel at a velocity equal to the speed of light, c.

Reference 6 solves the problem of the fields radiated by a current traveling at a constant velocity along an arbitrarily oriented line segment

(i. e., an idealized transmission line model) above a perfectly conducting earth. Details of this type of current model are given in Section 1.1 below. Only one sample waveform is presented as compared to the rather large collection of parameter variations presented by References 7 through 9. Perhaps the lack of examples is due to the strictly numerical method used for the multi-dimensional line integration.

References 7 through 9 present a concise development of the lightning return stroke current model as a current traveling along a series of straight-line segments. The earth is modeled as a perfect conductor. They present an exact analytic solution to this model for velocity of current propagation velocity $v = c$.

None of the above models use anything more complex than a perfectly conducting ground model. The theory of propagation of electromagnetic waves over a finitely conducting earth began with Reference 10 but there are more recent developments in References 11 through 14. Applications of this theory to the lightning return stroke modeled as an ideal current moment appear in References 15 through 17. In the rest of this note a model for a lightning return stroke is developed that considers both the effects of a finitely conducting ground and the effects of a reflection from the ionosphere. The source description is complex and consists of a known current propagating along a tortuous channel.

A frequency domain model for the perfectly conducting case is presented first, then the extension to finite ground conductivity is derived. An estimate of the reflection from the ionosphere is calculated using a one bounce approximation for frequencies above 1 kHz. Below that frequency propagation between the earth and ionosphere is treated using waveguide theory. The effect of the earth-ionospheric boundary is, in general, to attenuate certain frequencies. The concept of an signal function in which geometric factors have been removed, is useful for comparison with data.

Signal functions from the theoretical model are compared with integral transforms of experimental results. Finally, inverse transform techniques are used to study the distortion of transient waveforms by the environment surrounding the electromagnetic radiation.

The original contribution in this note is the combination of a complex return stroke model with an imperfectly conducting earth propagation model. The addition of the effects of the ionosphere to that model and the use of the model to interpret experimental data is also new.

1. THE PERFECTLY CONDUCTING EARTH

For simplicity, it is usually assumed that the earth is a perfect conductor when dealing with the propagation of lightning produced fields. For example, Reference 9 uses the image theory technique to calculate the fields from a geometrically complex return stroke model, including variations of velocity of propagation of the current pulse. The following derivation for a perfectly conducting earth follows their treatment closely. These results are later compared with more general analytical models where the effect of the finite ground conductivity is calculated.

1.1 The Current Model

The return stroke of a lightning flash discharges a charged conducting tortuous channel in the atmosphere. The leader channel appears optically to be a series of straight line segments which are connected to form the discharge path (Ref. 18). The diameter of the highly conducting channel is of the order of centimeters or less (Ref. 19) (while the corona radius is of the order of meters or greater) and the length of each line segment is about 50 m (Ref. 18). An analytical model of the return stroke current which is immediately appealing is that of a current pulse traveling along a path defined by a series of connected line segments leading from ground to cloud or from cloud to cloud. This model has discontinuities in path

direction which contribute significantly to the radiation (Refs. 7, 20). The corner formed by two intersecting channel segments is very sharp because of the small diameter of the current carrying channel. The discontinuities at the corner formed by the line segments in the model do not radiate much differently in the frequency range of interest ($\leq$ 10 MHz) than the actual corners. The number of line segments required for a given field calculation depends on observer distance and the highest frequency for which calculations of the fields are needed; but only a few segments provides a reasonable field prediction for most cases. The question of the number of segments required will be dealt with more quantitatively in Reference 21.

The shape of the current pulse traveling along the channel has been estimated from measurements of the current at the base of the channel (Refs. 18, 22). For convenience, the current pulse is usually described as a series of decaying exponentials (Ref. 18). For example, Reference 7 uses the following form for the current pulse.

$$f(t) = \left[I_0(e^{-\alpha t} - e^{-\beta t}) + I_1 e^{-\gamma t}\right]U(t) \qquad (1)$$

where U(t) is the unit step function. Values chosen for the coefficients and decay constants from the current at the base of the channel are (Ref. 7). These values are arbitrary and are only used by the model. A more complex model such as that of Reference 23 could as easily be introduced.

$I_0 = 30$ kA

$I_1 = 2.5$ kA

$\alpha = 2. \times 10^4$ sec^{-1}

$\beta = 2. \times 10^5$ sec^{-1}

$\gamma = 1. \times 10^3$ sec^{-1}

The first two exponentials represent the main current pulse, and the third exponential allows the addition of a slow bleed off of charge. Reference 24 uses a similar type of exponential series to represent the current pulse. These representations have the difficulty that the derivative of the current pulse has a maximum at t = 0 and is discontinuous there. In the LeVine and Meneghini model the current pulse itself has discontinuity at t = 0. References 25, 26 have measurements of the fields which indicate very fast rise times for the fields, but they have not generated equivalent possible currents. Propagation path distortion (as modeled in this note) and slow instrumentation have masked this rapidly changing character of the fields in the past. In spite of the above difficulties this current model is used in this note so that comparisons with the LeVine-Meneghini field predictions may be made.

The current pulse itself is shown in Figure 1. Note the non-zero value at t = 0. The pulse rise time is typically of the order of microseconds with a fall time of the order of hundreds of microseconds. This waveform is similar to measurements shown for the base of a channel (Ref. 22). These measurements are usually distorted by the presence of towers on which the measuring devices are placed. Also, the inherent assumption that the current waveform propagates up the channel without distortion cannot be supported (Ref. 22).

The return stroke, as mentioned before, is the discharge of a pre-charged conducting channel. A simple but useful model of this process is that of a pre-charged transmission line discharging. Using this model the current pulse travels along the set of line segments without distortion (not correct, see above) at some constant velocity. The actual velocity of propagation of the current along the channel is not well known, but is believed to be about one third of the speed of light (Ref. 27).

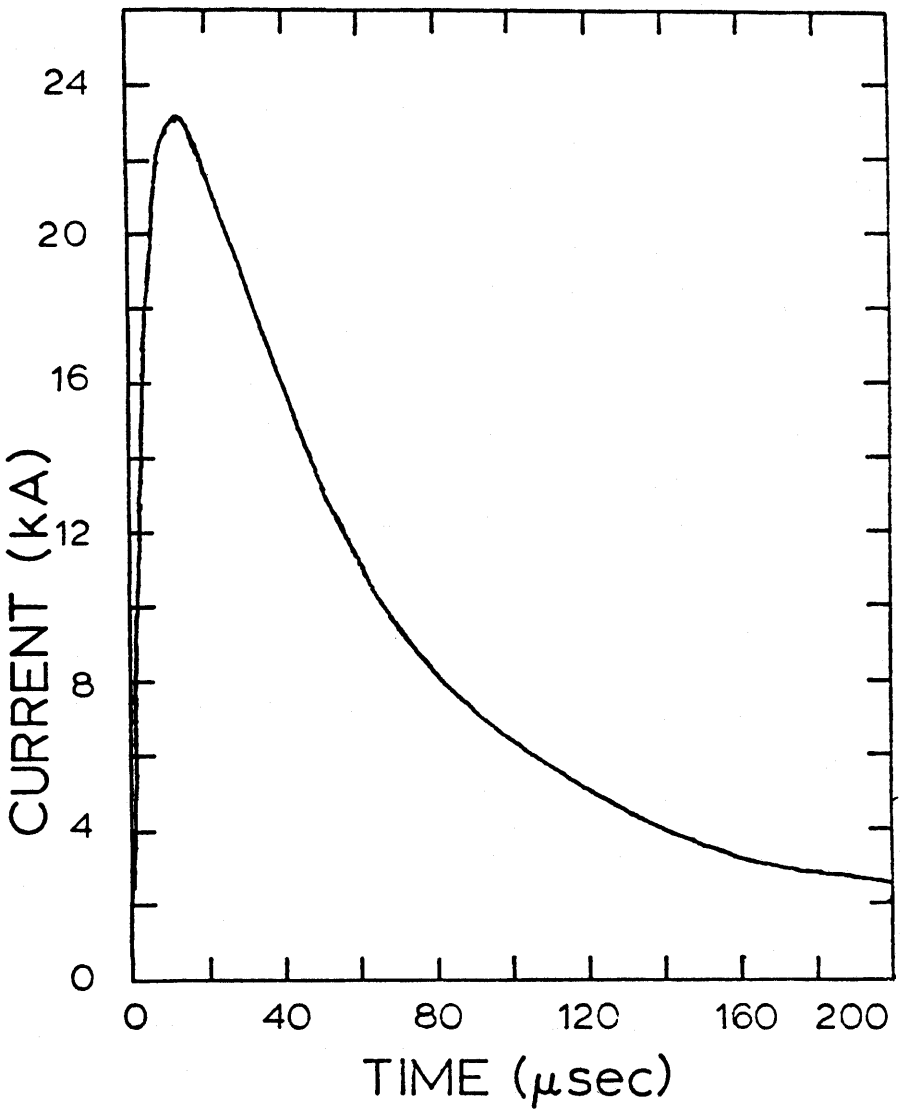

Figure 1. Transient waveform from model used by LeVine and Meneghini (Ref. 1). Waveform propagates along line segements.

The Fourier transform of the current pulse is given by:

$$\tilde{f}(\omega) = I_0\left[\frac{1}{i\omega+\alpha} - \frac{1}{i\omega+\beta}\right] + I_1\left[\frac{1}{i\omega+\gamma}\right] \qquad (2)$$

The Fourier transform $|\tilde{f}(\omega)|$ is shown in Figure 2 as a function of frequency. The spectrum is relatively constant at low frequencies and falls off as $1/\omega$ above about 10 kHz.

The Fourier transform in this part of the note is defined as

$$\tilde{f}(\omega) = \int_0^\infty f(t)e^{-i\omega t}\, dt$$

The lower limit is 0 since the function is defined as zero for $t \leq 0$. The inverse transform is given by

$$f(t) = \frac{1}{2\pi}\int_{-\infty}^{\infty} \tilde{f}(\omega)e^{i\omega t}\, d\omega$$

Later in the note the integration contour will be varied in these definitions for numerical convenience.

A spatially distributed and time dependent current is used to model the lightning return stroke in this note. The necessity for the details of the model is demonstrated in Reference 21 for several of the parameters in the current model and the propagation model developed in this note. This current model is now used to calculate electromagnetic fields for various geometries.

1.2 The Fields

The following derivation for the fields using a perfectly conducting ground assumption follows Reference 7 closely and is included because their

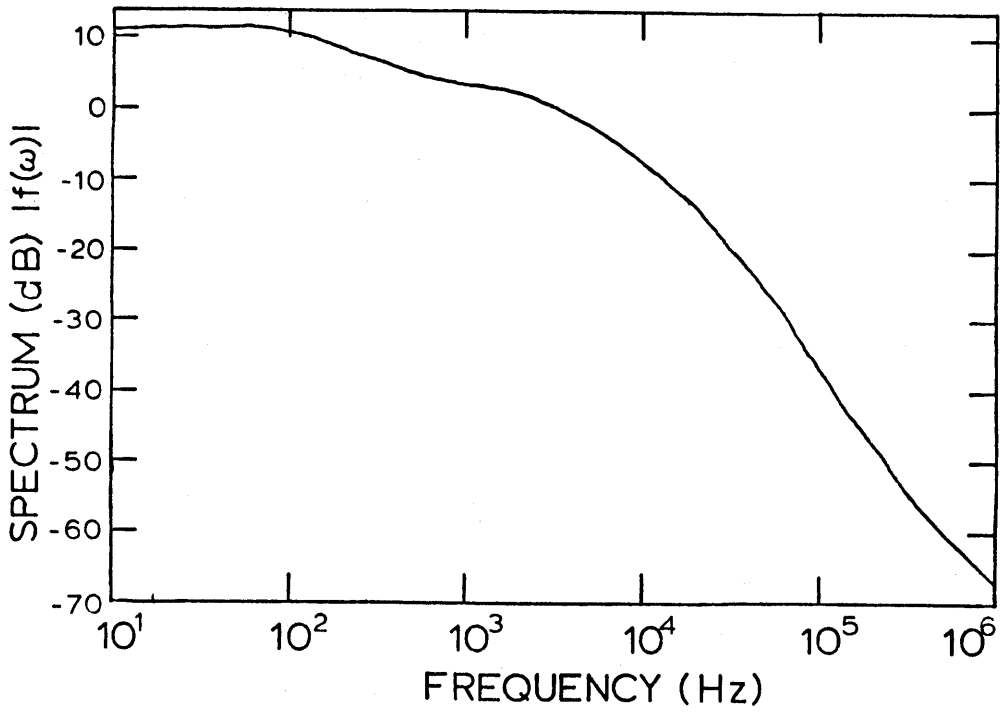

Figure 2. Fourier transform of return stroke current pulse from Figure 1.

results are used extensively to show the effects ofthe imperfectly conducting ground and ionosphere. Assume the return stroke current on a segment can be modeled as a traveling pulse, i. e., a transmission line model.

$$\vec{J}(\vec{r}',t) = \hat{l} f\left[t - \frac{\hat{l}\cdot\vec{r}'}{v}\right] \tag{3}$$

where $\hat{l}$ is a unit vector directed along the line segment as in the section above. The segment begins at $\vec{r}' = \vec{r}_a'$ and continues to $\vec{r}' = \vec{r}_b'$. The geometry is shown in Figure 3. The vector potential is then an integral over the line source and its image.

$$\tilde{\vec{A}}(\vec{r},\omega) = \mu_0 \int_{segment} \tilde{f}(\omega) e^{-ik\eta\hat{l}\cdot\vec{r}'} \left[\hat{l}\frac{e^{-ik|\vec{r}-\vec{r}_s'|}}{4\pi|\vec{r}-\vec{r}_s'|} - \hat{l}'\frac{e^{-ik|\vec{r}-\vec{r}_s'|}}{4\pi|\vec{r}-\vec{r}_s'|}\right] d\vec{r}_s' \tag{4}$$

For a current propagation velocity v the propagation parameter η is given by $\eta = c/v$. The unit vector in the propagation direction $\hat{l}$ is l with corresponding image unit vector $\hat{l}'$. The reflection coefficients for this model have unit magnitude. The reflection coefficients for the tangential fields are negative as required to maintain zero tangential electric field. The electric field may be constructed from the vector potential.

$$\tilde{\vec{E}}(\vec{r}_0,\omega) = ikc\left[\tilde{\vec{A}}(\vec{r}_0,\omega) - \frac{1}{k^2}\nabla(\nabla\cdot\tilde{\vec{A}}(\vec{r}_0,\omega))\right] \tag{5}$$

For the propagation velocity of the current pulse equal to that of light ($\eta = 1$), the integration in Equation 4 is done analytically by Reference 7. The integration is performed by rotating the coordinates to a new set of coordinates in which the new z axis is parallel to the current filament. The substitution in Equation 4 is

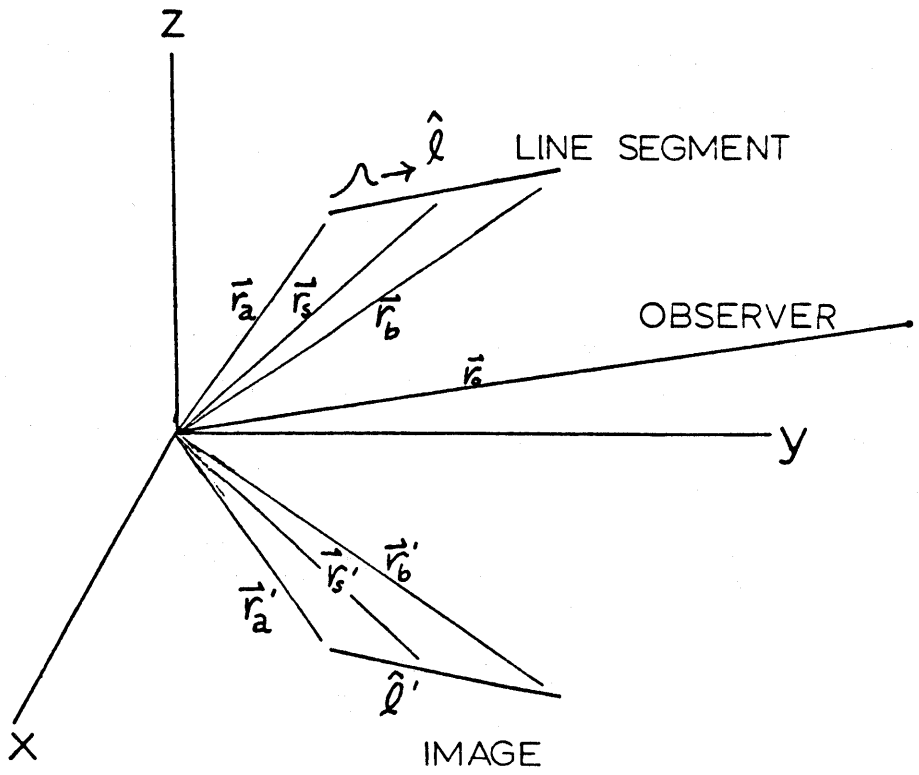

Figure 3. Geometry used in perfectly conducting earth solution. Waveform is shown propagating along line segment.

$$u = |\vec{r} - \vec{r}_s| + (\tilde{z}_s - \tilde{z}_0) \tag{6}$$

in the first integral and

$$u' = |\vec{r} - \vec{r}'_s| + (\tilde{z}'_s - \tilde{z}_0) \tag{7}$$

for the image term.

The tilde for this equation (and this equation only) represents the transformed coordinates and θ and ϕ are the angles of rotation in normal spherical coordinates. The tilde in any other equation indicates Laplace or Fourier transformed quantities. Transforming back to the original coordinates (Eq. 4) becomes

$$\tilde{\vec{A}}(\vec{r}_0,\omega) = \mu_0 \tilde{f}(\omega)\left\{\hat{l}\, e^{-ik\hat{l}\cdot\vec{r}_0} \int_{U(a)}^{U(b)} \frac{e^{-iku}}{4\pi u}\, du \right.$$

$$\left. - \hat{l}'\, e^{-ik\hat{l}'\cdot\vec{r}_0} \int_{U(a)'}^{U(b)'} \frac{e^{-iku'}}{4\pi u'} du' \right\} \tag{8}$$

where for m = a,b

$$U(m) = |\vec{r}_0 - \vec{r}_m| - \hat{l}\cdot(\vec{r}_0 - r_m)$$
$$U'(m) = |\vec{r}_0 - \vec{r}'_m| - \hat{l}'\cdot(\vec{r}_0 - r'_m) \tag{9}$$

and then $\vec{r}_m = \vec{r}_a, \vec{r}_b$ are the coordinates of the filament end points. Equation 9 denotes the location of the end points of the filaments and their images in the substitution (Eqs. 6, 7). Substituting Equation 8 into Equation 5 yields the electric field in the frequency domain.

$$\tilde{\vec{E}}(\vec{r}_0,\omega) = \left[\frac{\mu_0}{\varepsilon_0}\right]^{\frac{1}{2}} \tilde{f}(\omega)\left\{\left[\frac{e^{-ik\rho_b}}{4\pi\rho_b}\vec{\varepsilon}(\rho_b,\hat{l}) - \frac{e^{-ik\rho_a}}{4\pi\rho_a}\vec{\varepsilon}(\rho_a,\hat{l})\right]\right.$$
$$\left. - \left[\frac{e^{-ik\rho_b'}}{4\pi\rho_b'}\vec{\varepsilon}(\rho_b',\hat{l}') - \frac{e^{-ik\rho_a'}}{4\pi\rho_a'}\vec{\varepsilon}'(\rho_a',\hat{l}')\right]\right\} \tag{10}$$

where for m = a,b

$$\vec{\varepsilon}(\rho_m,\hat{l}) = e^{-ik\hat{l}\cdot\vec{r}_m}\left\{\left[\frac{1+\hat{l}\cdot\nabla\rho_m}{1-\hat{l}\cdot\nabla\rho_m}\right]^{\frac{1}{2}}\hat{\varepsilon}(\rho_m,\hat{l}) - i\frac{\nabla\rho_m}{k\rho_m}\right\} \tag{11}$$

and

$$\hat{\varepsilon}(\rho_m,\hat{l}) = \frac{\hat{l} - (\hat{l}\cdot\nabla\rho_m)\nabla\rho_m}{\left[1-(\hat{l}\cdot\nabla\rho_m)^2\right]^{\frac{1}{2}}} \tag{12}$$

and similarly for the image terms. The ρ_m are $\rho_m = \left|\vec{r} - \vec{r}_m\right|$ and $\rho_m' = \left|\vec{r} - \vec{r}_m'\right|$

The magnetic field may be obtained from $\tilde{\vec{H}} = \nabla \times \tilde{\vec{A}}$, but numerical values of the magnetic field were not required for this development.

Equation 10 is called the "exact solution" and is valid for all frequencies, but only for $\eta = 1$. For $\eta > 1$ the integral in Equation 4 can be performed only approximately. It is convenient in the derivation of the approximate solution to insert Equation 4 into Equation 5 prior to performing the integration. The result is

$$\tilde{\vec{E}}(\vec{r}_0,\omega) = -ik\left[\mu_0\right]^{\frac{1}{2}}\tilde{f}(\omega)\int_{filament} e^{-ik\eta(\hat{l}\cdot\vec{r}_0)}$$
$$\times\left\{\left[\hat{l} + \frac{1}{k^2}(\hat{l}\cdot\nabla)\nabla\right]\frac{e^{-ik\rho}}{4\pi\rho}d\rho\right.$$
$$\left. - \left[\hat{l}' + \frac{1}{k^2}(\hat{l}'\cdot\nabla)\right]\frac{e^{-ik\rho'}}{4\pi\rho'}d\rho'\right\} \tag{13}$$

where $\rho = \left|\vec{r} - \vec{r}_s\right|$ and $\rho' = \left|\vec{r} - \vec{r}'_s\right|$

The source-observer distance may then be expanded around the coordinates of the center of the filament $\vec{r}_c$.

$$\rho = |\vec{r} - \vec{r}_s| = |(\vec{r} - \vec{r}_c)| + |(\vec{r}_c - \vec{r}_s)|$$

$$\approx |\vec{r}_0 - \vec{r}_c| + |\vec{r}_c - \vec{r}_s|\cos(\varphi) + \frac{1}{2}\left[\frac{|\vec{r}_0 - \vec{r}_c|^2}{|\vec{r}_0 - \vec{r}_c|}\right] \tag{14}$$

where ϕ is the angle between filament and the vector from observer to the filament center or:

$$\cos(\varphi) = \frac{(\vec{r}_0 - \vec{r}_c)\cdot(\vec{r}_c - \vec{r}_s)}{|\vec{r}_0 - \vec{r}_c|\ |\vec{r}_c - \vec{r}_s|} \tag{15}$$

If $kL^2/\rho_C \ll 1$ and $kL \gg 1$ where L is the length of the filament and $\rho_C = \left|\vec{r} - \vec{r}_c\right|$, then the second term of Equation 14 may be dropped. Since the phase, in Equation 13 is more rapidly varying than the geometric factors ρ_C may be replaced by

$$\rho = \rho_c + |\vec{r}_c - \vec{r}'|\cos(\varphi)$$

in the exponential and $\rho = \rho_C$ elsewhere.

Then Equation 13 becomes

$$\vec{E}(\vec{r}_0,\omega) = -ik\left[\frac{\mu_0}{\varepsilon_0}\right]^{\frac{1}{2}}\tilde{f}(\omega)\left\{\left[\hat{l} + \frac{1}{k^2}(\hat{l}\cdot\nabla)\nabla\right]\frac{e^{-ik\rho_c}}{4\pi\rho_c}I(\omega)\right.$$

$$\left. - \left[\hat{l}' - \frac{1}{k^2}(\hat{l}'\cdot\nabla)\nabla\right]\frac{e^{-ik\rho'_c}}{4\pi\rho'_c}I'(\omega)\right\} \tag{16}$$

where

$$I(\omega) = \int_{filament} \exp\left[-ik\left(\eta(\hat{l}\cdot\vec{r}_s) + |\vec{r} - \vec{r}_s|\cos(\varphi)\right)\right] d\vec{r}_s \tag{17}$$

and similarly for the image term.

This integration may be performed in the same way as the vector integration for the $\eta = 1$ case. The result is:

$$I(\omega) = e^{-ik\eta\hat{l}\cdot\vec{r}_c}\left\{L\ \mathbf{sinc}\left[\frac{1}{2}kL(\eta - \hat{l}\cdot\nabla\rho_c)\right]\right\} \tag{18}$$

where $\mathrm{sinc}(z) = \sin(z)/z$

The derivative operations may be carried through in Equation 16 as

$$\left[\hat{l} + \frac{1}{k^2}(\hat{l}\cdot\nabla)\nabla\right]\frac{e^{-ik\rho_c}}{4\pi\rho_c} = \frac{i}{k\rho_c}\hat{l}\left[1 - \frac{i}{k\rho_c} - \frac{1}{(k\rho_c)_2}\right]$$
$$- \left[1 - \frac{3i}{k\rho_c} - \frac{3}{(k\rho_c)_2}\right](\hat{l}\cdot\nabla\rho_c)\nabla\rho_c\Bigg\}\frac{e^{-ik\rho_c}}{4\pi\rho_c} \tag{19}$$

The approximate solution is then

$$\tilde{\vec{E}}(\vec{r}_0,\omega) = -ik\left[\frac{\mu_0}{\varepsilon_0}\right]^{\frac{1}{2}}\tilde{f}(\omega)\left\{\hat{l}\left[1 - \frac{i}{k\rho_c} - \frac{1}{(k\rho_c)^2}\right]\right.$$
$$\left. - \left[1 - \frac{3i}{k\rho_c} - \frac{3}{(k\rho_c)^2}\right](\hat{l}\cdot\nabla\rho_c)\nabla\rho_c\right\}\frac{e^{ik\rho_c}}{4\pi\rho_c}I(\omega) \tag{20}$$

+ image terms.

If only the terms proportional to $1/k\rho_c$ are retained in Equation 20 the far field solution is obtained. The exact and far field solutions may be compared in Figures 4-6 for a vertical return stroke model with $\eta = 1$, $\vec{r}_a = (0,0,0)$ and $\vec{r}_b = (0,0,1500)$ meters. The observer is located at 5, 50, and 500 km distant from the source along the x-axis. For an increasing

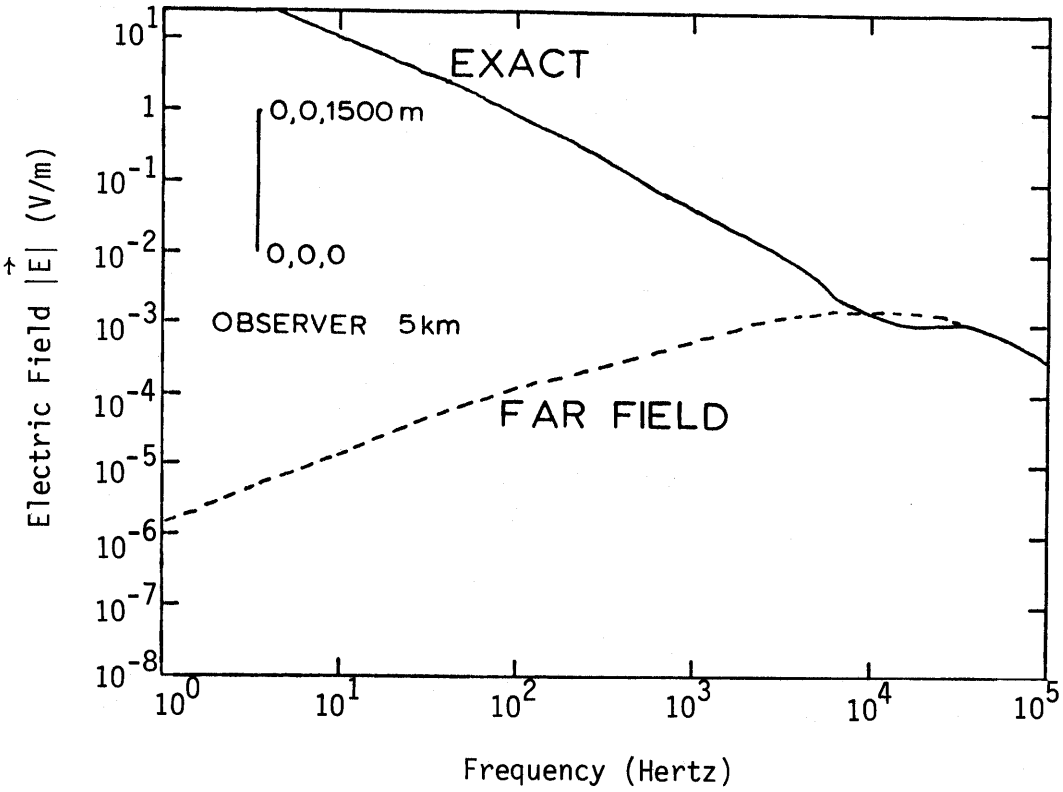

Figure 4. Electric field spectrum 5 km from return stroke over perfectly conducting ground. Return stroke channel is 1.5 km vertical column. Exact solution curve is exact electromagnetic solution for assumed current and return stroke geometry.

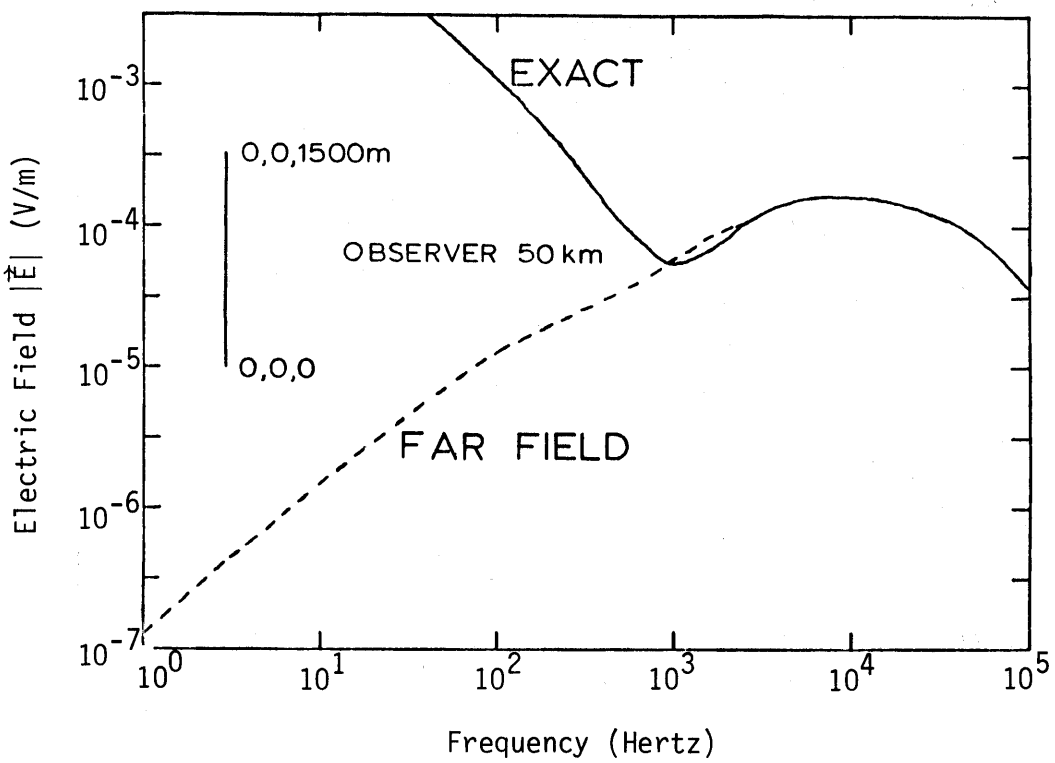

Figure 5. Electric field spectrum 50 km from return stroke over perfectly conducting ground. Return stroke channel is 1.5 km vertical column. Exact solution curve is exact electromagnetic solution for assumed current and return stroke geometry.

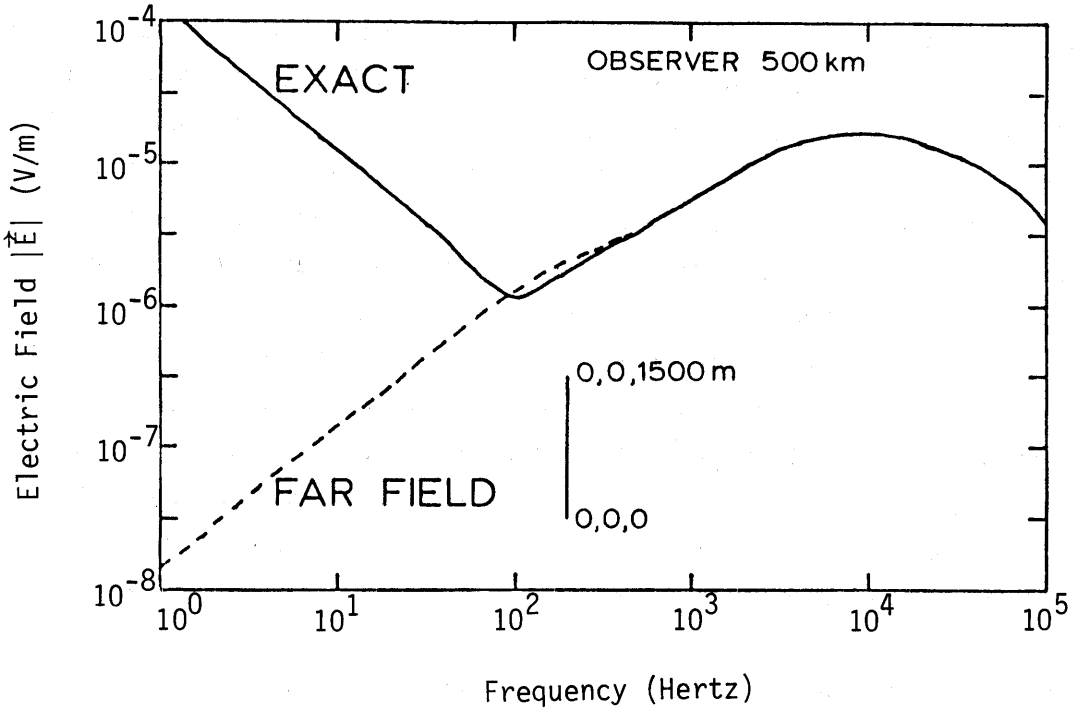

Figure 6. Electric field spectrum 500 km from return stroke over perfectly conducting ground. Return stroke channel is 1.5 km vertical column. Exact solution curve is exact electromagnetic solution for assumed current and return stroke geometry.

distance the quasi-static (proportional to 1/f) contribution becomes less important and the radiated field (proportional to f until the source roll-off becomes significant) becomes more dominant. The approximate solution is identical to the exact or complete solution for these distances. Equations 20 and 10 give essentially the same results as close as 2 km. The divergence between them at a distance of 1.5 km is shown in Figure 7. The importance of the close agreement of the approximate and exact solutions becomes apparent in the section on finite earth conductivity. In general, the effect of the finitely conducting earth is to attenuate frequencies above about 10 kHz for most example geometries. At frequencies below 1 kHz the earth is essentially a perfect conductor. The solution for a finitely conducting earth presented in t he next section then must approach the perfectly conducting earth solution at low frequencies and indeed closely matches the approximate (Eq. 20) solution at those low frequencies.

The effect of the velocity of propagation on the spectrum for the perfectly conducting earth case may be determined from Equation 20. The effect of a velocity of propagation of the current pulse less than c, $\eta > 1$, is to shift the nulls of the spectrum toward lower frequencies. This "spectral compression" also has the effect of attenuating higher frequencies. The effect of various propagation velocity parameters is shown in Figure 8. The spectra are only plotted to the first null for economy so the spectral compression is evident but the high frequency behavior of the fields is not. The variation of η and its effect on the fields is explored further in Reference 21. The return stroke channel model for Figure 8 is the same as that for Figures 4-7. The observer is 500 km away.

2. EFFECT OF AN IMPERFECTLY CONDUCTING GROUND

The effect of the environment on electromagnetic waves transmitted by a lightning return stroke consists of two parts at frequencies above about 1

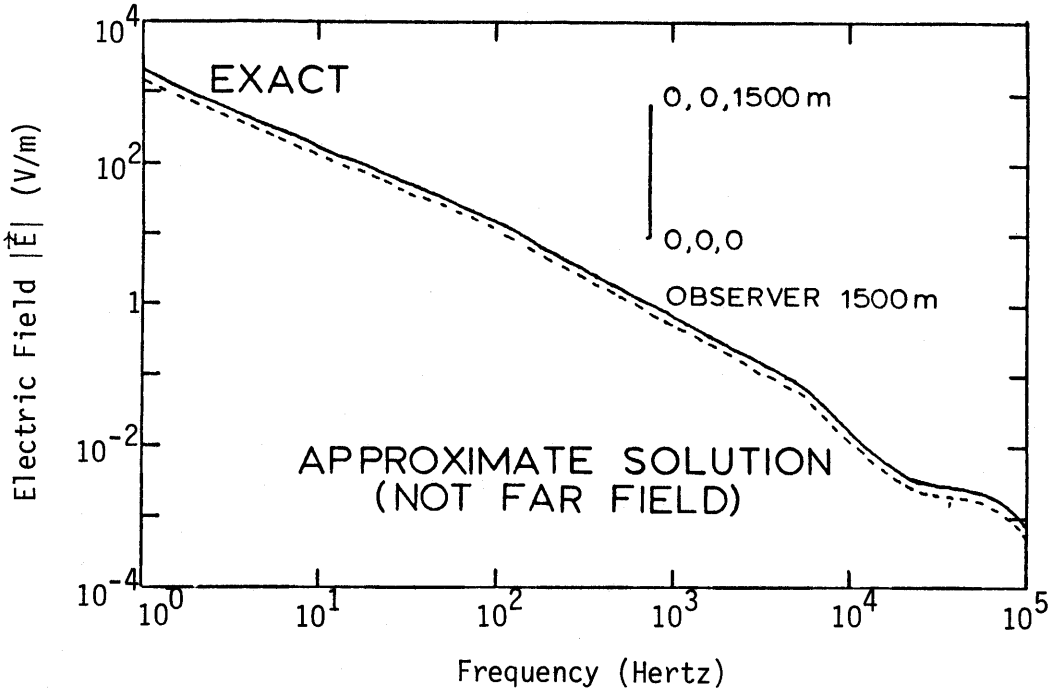

Figure 7. Nearby electric field spectrum showing close agreement of approximate and exact solutions. Exact solution is an exact electromagnetic solution for an assumed current and 1.5 km vertical column for a return stroke model.

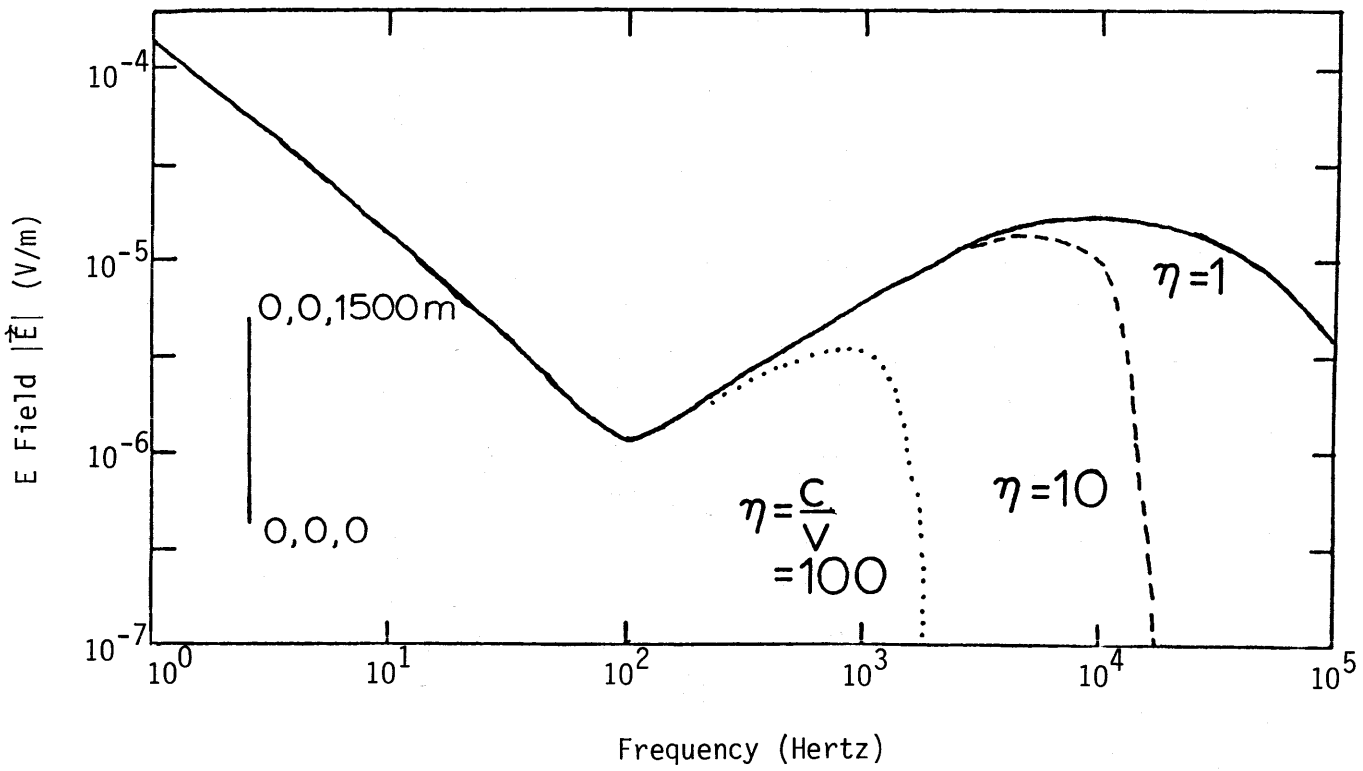

Figure 8. Electric field spectrum showing effects of variation of current pulse propagation velocity to first null only. Return stroke channel is modeled as a 1.5 km vertical column.

kHz. The most important effect is the attenuation due to an imperfectly conducting ground. The second contribution is due to reflection from the ionosphere and is generally much smaller than the ground wave (i. e., everything but the signal reflected from the ionosphere) since the signal is attenuated by distance in the frequency domain and delayed and attenuated for transient solutions. The reflected fields from the ionosphere are calculated in Section 3. A qualitative description of the importance of the addition of complexities to propagation models is given in Reference 28. Below about 1 kHz the signal wavelengths are larger than the earth-ionospheric separation and thus must be treated as a waveguide. The waveguide solution is described in Section 4.

Propagation of electromagnetic fields in the earth-ionospheric waveguide is the subject of extensive literature. The usual method of solving the propagation problem along an interface between earth and air is to use the Sommerfeld integral approach. Reducing the problem to an integral solution is straightforward, but the evaluation of the Sommerfeld integrals is more difficult. Reference 11 devotes a volume to a catalog of various approximations of the integrals, but evaluates none of them. References 13, 14, and 29 provide solutions to a large number of propagation problems in layered media, including the earth-ionospheric waveguide. The following derivation of the ground wave is a combination of the results of both texts but depends most strongly on the results of Reference 13.

The geometry for this problem is essentially the same as that in Figure 3 but now the parameters of the earth are finite. To help keep the indices straight the new geometry is shown in Figure 9. The upper medium is air and has permeability $\mu_2 = \mu_0$, conductivity $\sigma = 0$, and permittivity $\varepsilon_2 = \varepsilon_0$. It is denoted as medium 2 and the appropriate propagation constant is $k_2 = \omega(\mu_2\varepsilon_2)^{\frac{1}{2}}$. The lower medium is earth with permittivity ε_1, permeabilty $\mu_1 = \mu_0$, and conductivity σ_1. The appropriate propagation constant is

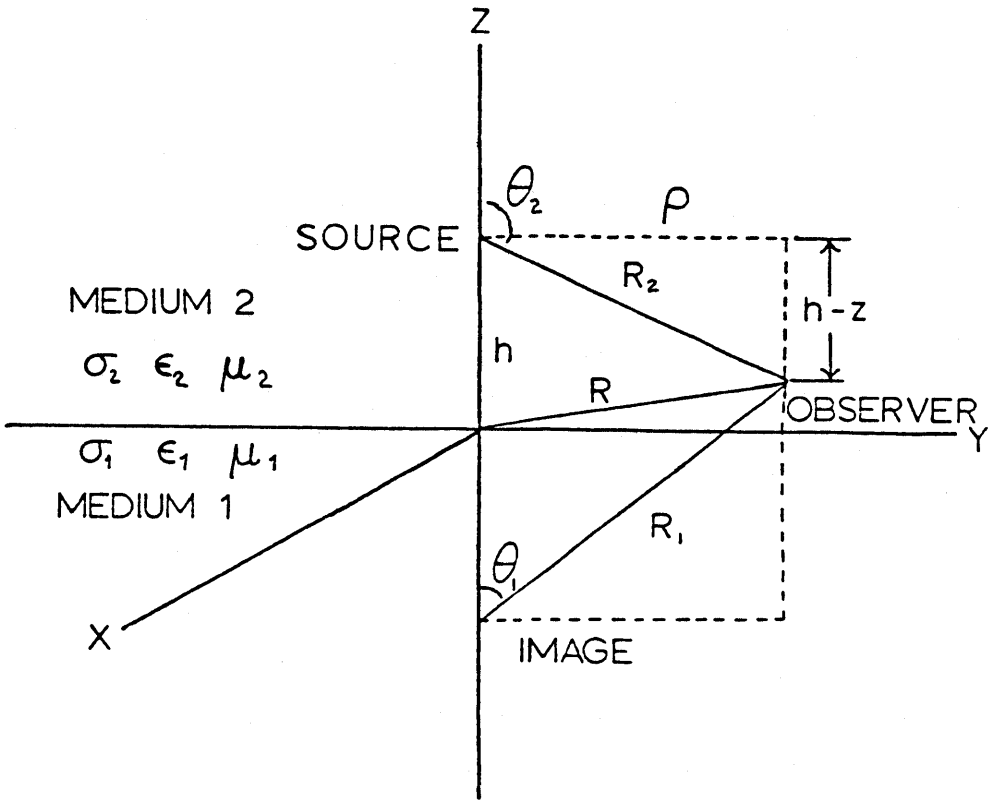

Figure 9. Geometry used in imperfectly conducting earth calculation of ground wave.

$$k_1 = (\omega^2 \mu_1 \varepsilon_1 - i\omega\mu_1\sigma_1)^{\frac{1}{2}} \tag{21}$$

In the formulation for the imperfectly conducting earth the lightning return stroke channel is again modeled by a series of line segments or filaments. However, each filament is decomposed into three dipoles, for convenience, each of which is treated as a separate transmitter, one parallel to each of the three cartesian unit vectors. The filament integration of each source is then performed in the same way as that of the approximate solution in the last section. The current pulse propagation velocity v is also decomposed into three cartesian components. As the current pulse propagates along the channel from filament to filament the phase is corrected using the filament midpoint as a reference. As a way of organizing the derivation, the fields for an ideal dipole are determined first. These results are then integrated to form the extended source results.

The $\hat{z}$ directed dipole is known as a vertical electric dipole (VED) and is the simplest to calculate of the two possible orientations (The third case can be found by rotation of the observation point by 90° parallel to the ground). Since only $\hat{z}$ directed currents are involved in the VED problem only a z-component of a Hertz vector $\tilde{\Pi} = \hat{z}\tilde{\Pi}_z$ is required to match the boundary conditions. The Hertz vector above the interface consists of a primary contribution, Π_z^P, from the dipole and a scattered contribution from the interface, Π_z^S. Then, the total Hertz vector is $\Pi_z^P + \Pi_z^S$. The primary field is just the field of a dipole in free space. The appropriate Hertz potential is

$$\tilde{\Pi}_z = \frac{\tilde{f}(\omega) L_z}{4\pi i \omega \varepsilon_0} \frac{e^{-ik_2 R_2}}{R_2} \tag{22}$$

where $R_2 = [\rho^2 + (z - h)^2]$ and L_z is the length of the dipole z component.

Equation (22) can be written in Sommerfeld integral form.

$$\tilde{\Pi}_z^P = \frac{\tilde{f}(\omega)L_z}{4\pi i\omega\varepsilon_0}\int_0^\infty J_0(\lambda\rho)e^{-u_2|z-h|}\lambda/u_2\, d\lambda \tag{23}$$

where $u_m = (\lambda^2 - k_m^2)^{\frac{1}{2}}$, m = 1,2. The sign of the square root is chosen, by convention, so that the real part is positive and thus insures convergence of the integral. The Bessel function of the first kind is denoted by $J_0(\lambda\rho)$. The reflected fields can be represented by

$$\tilde{\Pi}_z^S = \frac{\tilde{f}(\omega)L_z}{4\pi i\omega\varepsilon_0}\int_0^\infty \tilde{R}(\lambda)e^{-u_2(z+h)}\frac{\lambda}{u_2}d\lambda \tag{24}$$

where $R(\lambda)$ is an undetermined coefficient. The Hertz vector for $z > 0$ then is

$$\tilde{\Pi}_z = \tilde{\Pi}_z^P + \tilde{\Pi}_z^S \qquad z>0$$

The Hertz vector for $z < 0$, or for the fields in the ground can be represented by

$$\tilde{\Pi}_z = \frac{\tilde{f}(\omega)L}{4\pi i\omega\varepsilon_0}\int_0^\infty T(\lambda)J_0(\lambda\rho)e^{u_1(z-h)}\frac{\lambda}{u_2}d\lambda$$

$$,z<0 \tag{25}$$

where $T(\lambda)$ is an undetermined transmission coefficient. The electric fields must be continuous across the interface, or equivalently

$$k^2\tilde{\Pi}_z\Big|_{z=0^+} = k^2\tilde{\Pi}_z\Big|_{z=0}$$

and

$$\frac{\partial\tilde{\Pi}_z}{\partial z}\Big|_{z=0^+} = \frac{\partial\tilde{\Pi}_z}{\partial z}\Big|_{z=0^-} \tag{26}$$

Since these conditions must hold for all ρ, the following equations result.

$$k_2^2 e^{-u_2 h} + k_2^2 e^{-u_2 h} R(\lambda) = k_1^2 T(\lambda) e^{-u_1 h}$$

and

$$u_2 e^{-u_2 h} - u_2 R(\lambda) e^{-u_2 h} = u_1 T(\lambda) e^{-u_1 h} \tag{27}$$

These two equations may be solved for $R(\lambda)$. Since only the fields above the interface are of interest, $T(\lambda)$ is not required. The result is

$$R(\lambda) = -\frac{k_1^2 u_2 - k_2^2 u_1}{k_1^2 u_2 + k_2^2 u_1} \tag{28}$$

The reflection coefficient $R(\lambda)$ may be decomposed two different ways to achieve two ways of presenting the results. The first is

$$R(\lambda) = -\frac{k_1^2 u_2 + k_2^2 u_1}{k_1^2 u_2 + k_2^2 u_1} + \frac{2k_1^2 u_2}{k_1^2 u_2 + k_2^2 u_1} \tag{29}$$

Inserting this result in (24) yields

$$\tilde{\Pi} = \frac{\tilde{f}(\omega) L}{4\pi i \omega \varepsilon_0} \left\{ \frac{e^{-ik_2 R_2}}{R_2} - \frac{e^{-ik_2 R_1}}{R_1} + k_1^2 V \right\} \tag{30}$$

where

$$V = \int_0^\infty \frac{2\lambda}{k_1^2 u_2 + k_2^2 u_1} e^{-u_2(z+h)} J_0(\lambda\rho)\, d\lambda \tag{31}$$

This V is one of the fundamental integrals used in Baños' development of this problem. The integral also appears in the horizontal electric dipole (HED) problem and in the analogous magnetic dipole problems. A feature of this presentation is that the contribution from the two free space Green's functions cancel for observation points on the interface. In the

quasi-static limit (i. e., $k_2 \to 0$, k_1 remains finite) the reflection coefficient $R(\lambda) \to 1$ and $k_1^2 V$ approaches twice the free space Green's function from the image, as it must.

Another way of decomposing $R(\lambda)$ is

$$R(\lambda) = \frac{k_1^2 u_2 + k_2^2 u_1}{k_1^2 u_2 + k_2^2 u_1} - \frac{2k_1^2 u_2}{k_1^2 u_2 + k_2^2 u_1} \tag{32}$$

In this case

$$\tilde{\Pi}_z = \frac{\tilde{f}(\omega) L}{4\pi i \omega \varepsilon_0} \left\{ \frac{e^{-ik_2 R_2}}{R_2} + \frac{e^{-ik_2 R_1}}{R_1} - 2P \right\} \tag{33}$$

where

$$P = \int_0^\infty \frac{k_2^2 u_1}{k_1^2 u_2 + k_2^2 u_1} e^{-u_2(z+h)} \frac{\lambda}{u_2} J_0(\lambda\rho)\, d\lambda \tag{34}$$

In Equation 33 the perfectly conducting result appears in the two Green's functions and the term 2P forms a correction to the perfectly conducting result. This form is particularly applicable to this problem since earth is nearly perfectly conducting throughout the frequency range of interest.

The remaining problem is to perform the integration in Equation 31 or Equation 34. The two integrals are related so only one derivation is needed. Reference 13 demonstrates a compact form of the integration. A couple of definitions are required first to demonstrate the general applicability of the integral form of the Hertz vector.

Let Δ and Z_1 be defined by

$$\Delta = Z_1/\eta_0 = u_1/(\sigma_1 + i\omega\varepsilon_1) \tag{35}$$

where

$$\eta_0 = \left(\mu_0/\varepsilon_0\right)^{\frac{1}{2}}$$

is the impedance of free space. The quantity Z_1, then represents the surface impedance of the lower medium (Ref. 13). The impedance Z_1 is just the ratio of the tangential fields at the earth's surface.

$$Z_1 = -E_x/H_y\Big|_{z=0} \tag{36}$$

Continuity of the tangential fields is then equivalent to requiring the continuity of the impedance across the interface z = 0. The impedance concept is analogous to the similar development for transmission lines, but the impedance in a circuit is the ratio of a voltage to current rather than electric field (V/m) to magnetic field (A/m) as in the fields problem (Ref. 30). Equation 35 is only valid for the vertical polarization used here, but an similar result holds for the horizontal electric dipole. The reason for introducing the impedance concept is that it contains all the required information about the material below the interface to determine the reflection from that surface, no matter how complex. Suppose it is necessary to use a multi-layered earth model, rather than the homogeneous model used here. The quantity, $Z_1(\lambda)$ is all that is needed to determine the reflection coefficient from the lower medium. One must then do the non-trivial integral (Eq. 23) and of course this sequence of calculation is equivalent to any other way of solving the complete boundary value problem.

After this diversion P may be written using the impedance notation as

$$P = \int_0^\infty \frac{ik_2\Delta e^{-u_2(z+h)}}{(u_2 + ik_2\Delta)} \frac{\lambda}{u_2} J_0(\lambda\rho)\, d\lambda \tag{37}$$

The evaluation of the integral P will require the following assumptions.

(1) $|\Delta|^2 \ll 1$ and

$$0 < arg\,\Delta < \frac{\pi}{4}$$

These conditions are normally met in a highly conducting homogeneous earth model.

(2) $k_2\rho \gg 1$, This far field condition is not always physically met, so other methods will be needed to calculate the fields when this condition is not met. Fortunately, this condition is not too restrictive.

The details of the integration (Eq. 37) are contained in Reference 14. The method used is that of steepest descents. The method of steepest descents is a technique for finding the asymptotic value of integrals of the form (Ref. 31).

$$I(x) = \int_C h(t)e^{x\rho(t)}dt \tag{38}$$

where h(t) and $\rho(t)$ are analytic functions of t. It is required generally that x be a large parameter. The large parameter role is played by $k_2\rho$

in Equation 37. The contour C is distorted to a new contour on which $\rho(t)$ has a constant imaginary part to eliminate rapid oscillations when t is large. In the distortion of the contour contributions from poles and branch cuts must be correctly considered. It is then assumed that the integral only has a major contribution near a maximum of Real $(\rho(t))$ at $t = c$. The function h(t) may then be expanded around $t = c$, and the integration carried out term by term. The point c is known as a saddle point. Frequently, only the first term approximation $h(t) = h(c)$ is needed. When distorting the contour one must consider branch points and poles of h(t) and $\rho(t)$. In particular a pole near the saddle point can severely restrict the radius of convergence of the asymptotic series (Ref. 11). To extend the validity of this series the pole should be treated separately. In the case of the integral P there is a pole near the saddle point. The integral is then evaluated by removing the slowly varying quantities from the integrand and evaluating the remaining integral, which contains the exponential and the term with the pole. This remaining integral can be evaluated analytically, in this case.

The result of these operations on Equation 37 yields the following approximate value of the integral (Ref. 13) for the assumptions about distance of the observer and ground conductivity stated above.

$$P = i\left[\pi p\right]^{\frac{1}{2}} e^{-w}\,\mathbf{erfc}(iw^{\frac{1}{2}})\frac{e^{-ik_2R_1}}{R_1} \tag{39}$$

where $\omega = p\left(1 + (h + z)/(\Delta R_1 2)\right)^2$ and $p = (-ik_2R_1)/(2)\Delta_2$ is the Sommerfeld Numerical Distance. The expression for P can also be written

$$P = \left(\frac{p}{w}\right)^{\frac{1}{2}}\left[1-F(w)\right]\frac{e^{-ik_2R_1}}{R_1} \tag{40}$$

where a method of calculating F(w) is given in Appendix B. Inserting Equation 40 into Equation 33 and comparing to Equation 30 yields for V.

$$k_1^2 V = 2(1-i\sqrt{\pi p}\,e^{-w}\,\mathbf{erfc}(iw^{\frac{1}{2}}))\frac{e^{-ik_2R_1}}{R_1} \tag{41}$$

The fields from the dipole are given by

$$\tilde{E}_r = -\frac{i\omega\tilde{f}(\omega)L_z\mu_0}{4\pi k_2^2}\left\{\frac{\partial^2}{\partial r\,\partial z}\left[\frac{e^{-ik_2R_2}}{R_2} - \frac{e^{-ik_2R_1}}{R_1} + k_1^2V\right]\right\} \tag{42}$$

$$\tilde{E}_z = -\frac{i\omega\tilde{f}(\omega)L_z\mu_0}{4\pi k_2^2}\left\{\left[\frac{\partial^2}{\partial z^2} + k_2^2\right]\left[\frac{e^{-ik_2R_2}}{R_2} - \frac{e^{-ik_2R_1}}{R_1} + k_1^2V\right]\right\} \tag{43}$$

$$\vec{E}_\varphi = 0$$

and

$$\tilde{H}_\varphi = -\frac{\tilde{f}(\omega)L_z}{4\pi}\left\{\frac{\partial}{\partial r}\left[\frac{e^{-ik_2R_2}}{R_2} - \frac{e^{-ik_2R_1}}{R_1} + k_1^2V\right]\right\} \tag{44}$$

$$\vec{H}_r = \vec{H}_z = 0$$

These fields are for a point dipole. This solution may be used directly by always choosing the filaments of which the return stroke channel model is constructed to be much smaller than a wavelength. A numerically more efficient approach is to use the technique leading to (Eq. 20). To use this technique note that V contains a factor of $(e^{ik_2R_1})/(R_1)$. The remainder of V and the geometric part of the Green's function may be evaluated at the center coordinates of the filament. A better value for the fields allowing the use of longer filaments is:

$$\tilde{E}_r = -\frac{i\omega\tilde{f}(\omega)L_z\mu_0}{4\pi k_2^2}\left\{\mathbf{sinc}\left[\frac{1}{2}k_2L_z(\eta_z - (\nabla R_C)_z)\right]\frac{\partial^2}{\partial r\,\partial z}\frac{e^{-ik_2R_2}}{R_2}\right.$$

$$\left. - \mathbf{sinc}\left[\frac{1}{2}k_2L_z(\eta_z - (\nabla R_C')_z)\right]\frac{\partial^2}{\partial r\,\partial z}\left[\frac{e^{-ik_2R_1}}{R_1} + k_1^2V\right]\right\} \tag{45}$$

and

$$\tilde{E}_z = -\frac{i\omega\tilde{f}(\omega)L_z\mu_0}{4\pi k_2^2}\left\{\mathbf{sinc}\left[\frac{1}{2}k_2L_z(\eta_z - (\nabla R_C)_z)\right]\right.$$
$$\times\left[\frac{\partial^2}{\partial z^2} + k_2^2\right]\frac{e^{-ik_2R_2}}{R_2}$$
$$\left. - \mathbf{sinc}\left[\frac{1}{2}k_2L_z(\eta_z - (\nabla R_C)_z)\right]\left[\frac{\partial^2}{\partial z^2} + k_2^2\right]\left[\frac{e^{-ik_2R_1}}{R_1} - k_1^2V\right]\right\} \qquad (46)$$

where R_C and R_C' are the distances to the center of the filament and its image. The velocity parameter $\eta_Z = c/v_Z$, where v_Z is the vertical component of the current pulse propagation velocity and L_Z is the vertical extent of the filament. The correction factor varies very slowly with distance and so its derivatives do not contribute. It should be noted that (Eq. 46) represents the dominant part of the electric fields from a given filament. Proper evaluation of the derivative in (Eq. 46) gives a set of values for $\tilde{E}_Z$ valid over a similar range of parameters as the approximate solution (Eq. 20). Both (Eq. 20) and (Eq. 46) approximate the exact solution (Eq. 10) rather well at low frequencies. Equation (Eq. 46) was derived under the assumption $k_2\rho \gg 1$. However, the finitely conducting solution (Eq. 46) does not depart significantly from the perfectly conducting solution (Eq. 20) until the condition $k_2\rho \gg 1$ is met for a range greater than about 1 km. Therefore, (Eq. 46) is a reasonable approximation of the fields over a homogeneous conducting ground for frequencies from 1 kHz to several MHz and for ranges from 1 km to about 250 km. The upper range limit is required because the effects of earth curvature become important.

For the horizontal dipole it is sufficient to consider only the $\hat{x}$ directed components since, by symmetry of the interface, the $\hat{y}$ component can be obtained by rotating the observation point parallel to the ground 90°. For the $\hat{x}$ directed dipole (geometry still as in Figure 9) two com-

ponents are required for the Hertz vector to match the boundary conditions. While there are only horizontal driving currents there are also, of course, vertical currents induced in the ground. The Hertz vector is then

$$\tilde{\vec{\Pi}} = (\tilde{\Pi}_x, 0, \tilde{\Pi}_z) \tag{47}$$

The boundary conditions are that the tangential fields are continuous. This in turn requires that

$$\begin{aligned} k_1^2 \tilde{\Pi}_{1x} &= k_2^2 \tilde{\Pi}_{2x} \\ k_1^2 \frac{\partial}{\partial z} \tilde{\Pi}_{1x} &= k_2^2 \frac{\partial}{\partial z} \tilde{\Pi}_{2x} \\ k_1^2 \tilde{\Pi}_{1z} &= k_2^2 \tilde{\Pi}_{2z} \\ \frac{\partial}{\partial x} \tilde{\Pi}_{1x} + \frac{\partial}{\partial z} \tilde{\Pi}_{1z} &= \frac{\partial}{\partial x} \tilde{\Pi}_{2x} x + \frac{\partial}{\partial z} \tilde{\Pi}_{2z} \end{aligned} \tag{48}$$

where the integer subscript to the Hertz vector components indicates the region in which the component is evaluated. Using a similar set of integral forms for the Hertz vectors and applying the boundary conditions yields the following values for the electric fields in the air region due to an $\hat{x}$ directed dipole in air (Ref. 11)

$$\tilde{E}_r = -\frac{i\omega \tilde{f}(\omega) L_x \mu_0}{4\pi k_2^2} \cos(\varphi) \left\{ \left[\frac{\partial^2}{\partial r^2} + k_2^2 \right] \frac{e^{-ik_2 R_2}}{R_2} - \left[\left[\frac{\partial^2}{\partial r^2} + k_2^2 \right] \frac{e^{-ik_2 R_1}}{R_1} - k_2^2 \frac{\partial^2}{\partial r^2} V - k_2^2 U \right] \right\}$$

$$\tilde{E}_\varphi = -\frac{i\omega \tilde{f}(\omega) L_x \mu_0}{4\pi k_2^2} \sin(\varphi) \left\{ \left[\frac{1}{r} \frac{\partial}{\partial r} + k_2^2 \right] \frac{e^{-ik_2 R_2}}{R_2} - \left[\left[\frac{1}{r} \frac{\partial}{\partial r} + k_2^2 \right] \frac{e^{-ik_2 R_1}}{R_1} - k_2^2 \frac{1}{r} \frac{\partial}{\partial r} V - k_2^2 U \right] \right\}$$

and

$$\tilde{E}_z = -\frac{i\omega\tilde{f}(\omega)L_x\mu_0}{4\pi k_2^2}\cos(\varphi)\left\{\frac{\partial^2}{\partial r\,\partial z}\left[\frac{e^{-ik_2R_2}}{R_2}\right] + \left[\frac{\partial^2}{\partial r\,\partial z}\left[\frac{e^{-ik_2R_1}}{R_1} - k_1^2V\right]\right]\right\}$$

where the angle ϕ is the angle between the x-axis and the observer.

These fields for the horizontal dipole may be integrated over the finite extent of the line source. This integration is identical to the approximate source integration for the vertical dipole and explicitly described in Section 1 for the perfectly conducting ground. The perfectly conducting ground result is the same as in Reference 7. After the integration is performed the fields for the finite horizontal component of the line segment are

$$\tilde{E}_r = -\frac{i\omega\tilde{f}(\omega)L_x\mu_0}{4\pi k_2^2}\cos(\varphi)\left\{\left[\frac{\partial^2}{\partial r^2} + k_2^2\right]\frac{e^{-ik_2R_2}}{R_2}\mathbf{sinc}\left[\frac{1}{2}k_2L_x(\eta_x - (\nabla R_C)_x)\right] - \left[\left[\frac{\partial^2}{\partial r^2} + k_2^2\right]\frac{e^{-ik_2R_1}}{R_1} - k_2^2\frac{\partial^2}{\partial r^2}V - k_2^2U\right] \times \mathbf{sinc}\left[\frac{1}{2}k_2L_x(\eta_x - (\nabla R_C')_x)\right]\right\} \tag{49}$$

$$\tilde{E}_\varphi = -\frac{i\omega\tilde{f}(\omega)L_x\mu_0}{4\pi k_2^2}\sin(\varphi)\left\{\left[\frac{1}{r}\frac{\partial}{\partial r} + k_2^2\right]\frac{e^{-ik_2R_2}}{R_2}\mathbf{sinc}\left[\frac{1}{2}k_2L_x(\eta_x - (\nabla R_C)_x)\right] - \left[\left[\frac{1}{r}\frac{\partial}{\partial r} + k_2^2\right]\frac{e^{-ik_2R_1}}{R_1} - k_2^2\frac{1}{r}\frac{\partial}{\partial r}V - k_2^2U\right] \times \mathbf{sinc}\left[\frac{1}{2}k_2L_x(\eta_x - (\nabla R_C')_x)\right]\right\} \tag{50}$$

and

$$\tilde{E}_z = -\frac{i\omega\tilde{f}(\omega)L_x\mu_0}{4\pi k_2^2}\cos(\varphi)\left\{\frac{\partial^2}{\partial r\,\partial z}\left[\frac{e^{-ik_2R_2}}{R_2}\right]\mathbf{sinc}\left[\frac{1}{2}k_2L_x(\eta_x - (\nabla R_C)_x)\right]\right.$$

$$\left. + \left[\frac{\partial^2}{\partial r\,\partial z}\left[\frac{e^{-ik_2R_1}}{R_1} - k_1^2V\right]\mathbf{sinc}\left[\frac{1}{2}k_2L_x(\eta_x - (\nabla R_C')_x)\right]\right]\right\} \qquad (51)$$

The integral V is the same as in the VED case and U is a similar fundamental integral given by

$$U = \int_{-\infty}^{\infty}\frac{2e^{-u_2(z+h)}}{u_1 + u_2}H_0^{(1)}(\lambda\rho)\,\lambda d\lambda \qquad (52)$$

This integral can evaluated using steepest descents techniques, as well, but there is no pole to worry about in the integrand in (Eq. 52). Baños evaluates the integral under the conditions $e^{-ik_1\rho} \gg 1$ and $|\eta^2| = |k_2/k_1|^2 \ll 1$. Both these conditions are readily met for the usual earth parameters and range restrictions for the vertical dipole. Baños divides the calculation for U into two parts corresponding to integrations around the branch cuts for the branch points $\lambda = k_1$ and $\lambda = k_2$. The result is

$$U = U^{(1)} + U^{(2)}$$

The contribution $U^{(1)}$ is proportional to $e^{-ik_1\rho}$ and is therefore exponentially attenuated with distance and does not contribute for distances larger than a few hundred meters. The remaining $U^{(2)}$ contribution can be approximated for distances larger than a few hundred meters and for $n \ll 1$ by

$$U^{(2)} \approx \frac{2(1 + ik_1(z + h))}{k_1^2} \frac{1}{r} \frac{\partial}{\partial r} \left[\frac{e^{-ik_2 r}}{r} \right] \tag{53}$$

The value for U in (Eq. 53) is only valid for observation and source points near the interface because of the way Baños applies the steepest descent technique. In the model presented in this note no derivatives are taken of U. Derivatives are taken, however, of the expression for V. Baños derives an expression analogous to (Eq. 41) which is also to be used for observation points and source points near the interface. That expression is:

$$V \approx 2 \frac{Q^{-\frac{1}{2}}}{k_1^2 (1 - n^4) \rho} e^{ik_2 \rho} e^{-ink_0(z+h)}$$
$$\times \left\{ 1 - i\left(\frac{1}{2}\pi\right)^{\frac{1}{2}} x_0 e^{-x_0^2} \operatorname{erfc}(ix_0 / 2^{\frac{1}{2}}) \right\} \tag{54}$$

where $Q = 2n^{-2}[(1 - n_2)^{\frac{1}{2}} - 1]$

$$k_0 = k_2 / (1 + n_2)^{\frac{1}{2}}$$

and x_0 is defined using Baños representation for the Sommerfeld Numerical Distance.

$$p = \frac{1}{2} x_0^2 = -\frac{1}{2} i n^2 k_2 \rho (1 + n^2)^{-\frac{1}{2}} Q = -i(k_2 - k_0)\rho$$

One must be cautious when substituting this value for V into the field Equations 45-51 since limits as z becomes small have already been taken. The derivative with respect to z is proportional to n. The derivatives then vanish in the perfectly conducting limit, which is not correct. This behavior implies that $\tilde{E}_z$ for the HED vanishes for $n \to 0$. The fields in that case are small but do not vanish. The derivative must be

taken before the approximation for small z is made. Equation 41 may be substituted directly in the field equations and leads to the correct derivatives. Equation 41 is used in the numerical evaluation of the fields for examples using the model in this note.

This summary completes the ground wave portion of the field propagation model. The complete solution requires a calculation of reflection from the ionosphere.

3. THE SKY WAVE

The total electromagnetic field due to a source in the earth-ionospheric waveguide can considered as constructed of two parts. The first part is the direct wave with modification due to the presence of the ground as calculated in section 2. This part is known as the ground wave. The other part of the wave is that contribution that interacts with the ionosphere and is known as the sky wave. Further interactions may take place between the earth and ionosphere than the single bounce approximation used here but the effects are usually smaller than those calculated in the model. Multiple bounces may be included in a straightforward way.

The magnitude of the sky wave is usually significantly less than that of the ground wave for these reasons:

(1) The time of arrival of the sky wave is delayed by the additional travel time from the source to ionosphere to receiver.

(2) The additional path length allows additional geometric attenuation of the wave.

(3) At some frequencies the reflection coefficient for the ionosphere is significantly less than 1 and the majority of the wave is transmitted through the ionosphere rather than reflected to the receiver.

In this model the sky wave contribution is modeled using a single bounce theory with appropriate reflection coefficients used at the boundaries, as shown in Figure 10.

The single bounce model adds the contributions from those rays that bounce once from the ionosphere, including those that also bounce once from the ground, before reaching the observer.

The waves bouncing from the ground are modified by the appropriate Fresnel reflection coefficients. The waves bouncing from the ionosphere are also modified to account for the anisotropy of the ionosphere as in Reference 32.

Using the quasi-longitudinal (Refs. 33 and 35) approximation (vertical magnetic field and vertical propagation within the ionosphere), appropriate in the region of 70-90 km altitude where much of the reflection occurs, the complex refractive index μ of the ionosphere may be approximated as

$$\mu^2 \approx 1 - i(\omega_r/\omega)\exp(\pm i\tau) \tag{55}$$

where $\tan(\tau) = \omega_L/\nu$ and

$$\omega_r = \omega_0^2(\nu^2 + \omega_L^2)^{-\frac{1}{2}}$$

In the above ω_L is the cyclotron frequency, ν is the collision frequency and ω_0 is the plasma frequency. Numerical values for these constants are given in Section 4. The plus sign in (Eq. 55) corresponds to the refractive index for the ordinary ray and the refractive index for that case is

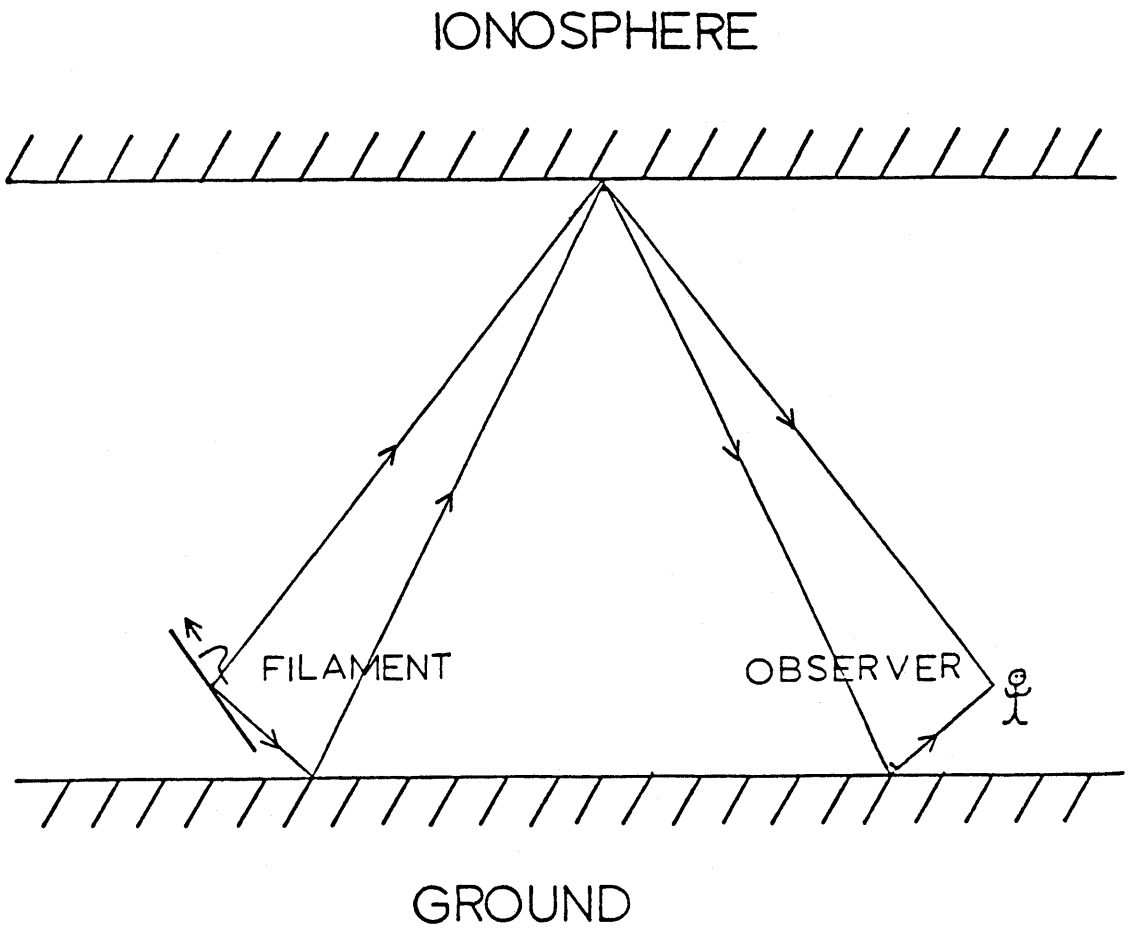

Figure 10. Geometry of sky wave problem showing rays contributing to sky wave.

denoted by μ_0. The negative sign corresponds to the extraordinary ray and is denoted by μ_0.

The reflection coefficients are determined by considering a plane wave incident on an ionospheric model with a step function boundary. The wave is incident at an angle ϕ with the vertical. The reflection coefficients are then obtained by matching tangential fields at the interface. The result is (Ref. 32)

$$
\begin{aligned}
{}_{\parallel}R_{\parallel} &= \Big\{(\mu_o + \mu_e)(C^2 - C_oC_e) \\
&+ (\mu_o\mu_e - 1)(C_o + C_e)C\Big\}/D \\
{}_{\parallel}R_{\perp} &= 2iC(\mu_oC_o - \mu_eC_e)/D \\
{}_{\perp}R_{\parallel} &= 2iC(\mu_oC_e - \mu_eC_o)/D \\
{}_{\perp}R_{\perp} &= \Big\{(\mu_o + \mu_e)(C^2 - C_oC_e) \\
&- (\mu_o\mu_e - 1)(C_o + C_e)C\Big\}/D
\end{aligned}
\tag{56}
$$

where

$$
\begin{aligned}
D &= (\mu_o + \mu_i)(C^2 + C_oC_e) \\
&+ (\mu_o\mu_e + 1)(C_o + C_e)C, \\
\mu_o\sin(\varphi_o) &= \mu_e\sin(\varphi_e) = \sin(\varphi)
\end{aligned}
$$

and

$$
C = \cos(\varphi), C_o = \cos(\varphi_o), C_e = \cos(\varphi_e)
$$

The subscripts on the reflection coefficients indicate reflection from one wave polarization to another. For example, R is the reflection coefficient representing that portion of a wave with electric field parallel to

the plane of incidence that is reflected with electric field perpendicular to the plane of incidence.

The real parts of the reflection coefficients for the ground are shown in Figure 11. The departure from perfect conductivity for the earth ($\sigma = 5 \times 10^{-3}$) mho/m does not occur until nearly 100 kHz.

The real parts of the reflection coefficients for the ionosphere are shown in Figure 12. At the 100 kHz point these coefficients have dropped severely. After 100 kHz the ionosphere has begun to be transparent and so the sky wave contribution is no longer significant. For these curves the angle of incidence is about 45°.

The effect of anisotropy is shown in Figure 13 and appears to become significant around 800 Hz, increasing to a maximum at about 100 kHz before the entire sky wave fades due to transparency. These reflection coefficients are based on a sharply bounded ionospheric model with collision frequency $\nu = 10^6$ s^{-1}, electron density $n = 10^8$ m^{-3} the longitudinal magnetic field $H_{long} = 5 \times 10^{-4}/\mu_0$ A/m.

Reflection from the ionosphere may be calculated for much more detailed models of the ionosphere. The slab model may be replaced with, for example, an exponential profile (Refs. 12, 35). The wave reflects from deeper in the ionosphere as frequency increases for a non-slab geometry. The exponential profile is in the wave number for the reflective boundary. The anisotropic nature of the ionosphere may be treated in a more detailed way without the quasi-longitudinal approximation (Ref. 36). The method described in this section for calculating the reflection from the ionosphere is intended only to provide an estimate of the reflection since the sky wave generally does not play a large part in the total field.

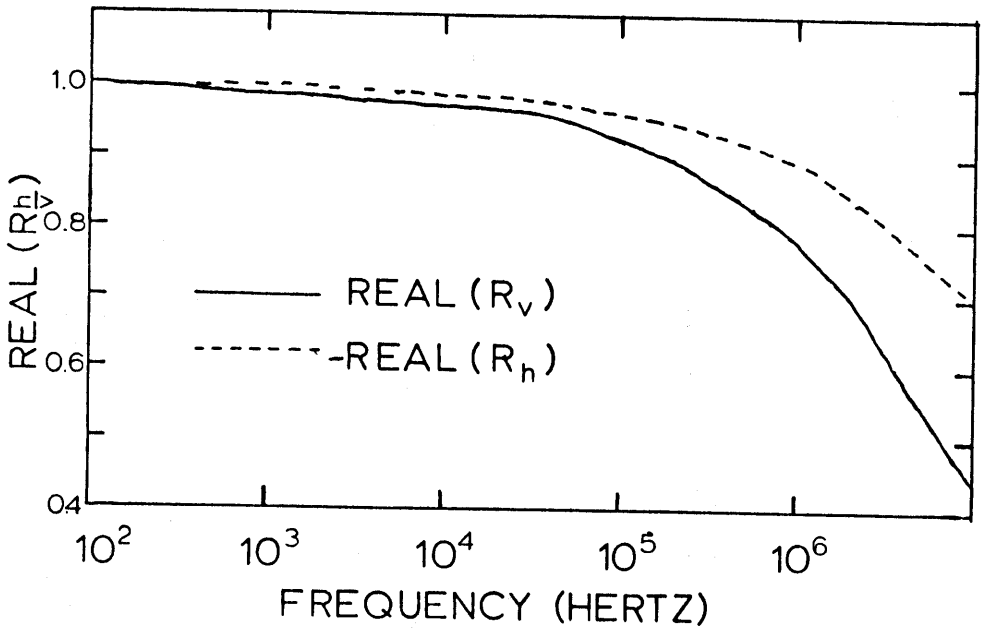

Figure 11. Reflection coefficients for reflection from ground as a function of frequency (R_h is horizontal polarization).

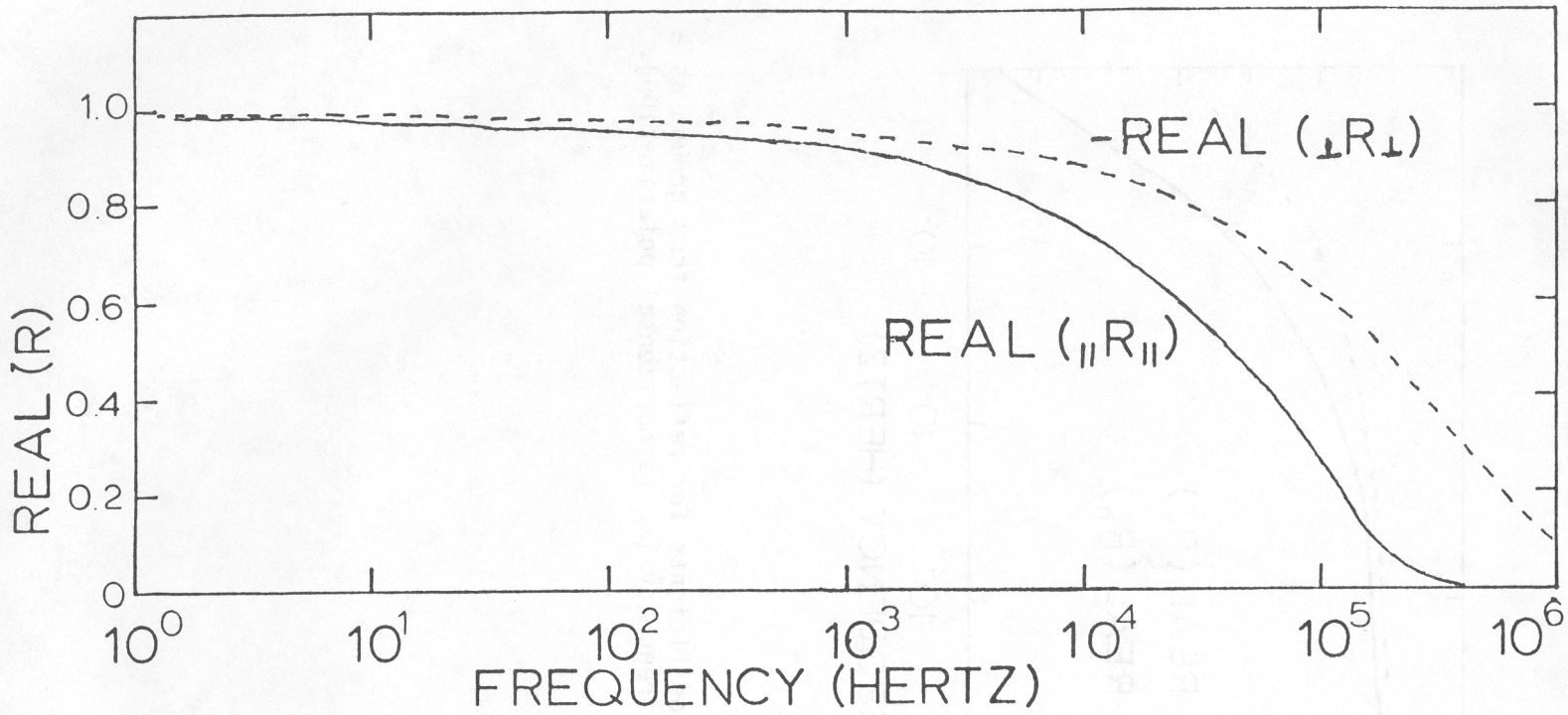

Figure 12. Reflection coefficients which maintain polarization for reflection of waves from ionosphere as a function of frequency. Slab ionosphere. See text for polarization notation.

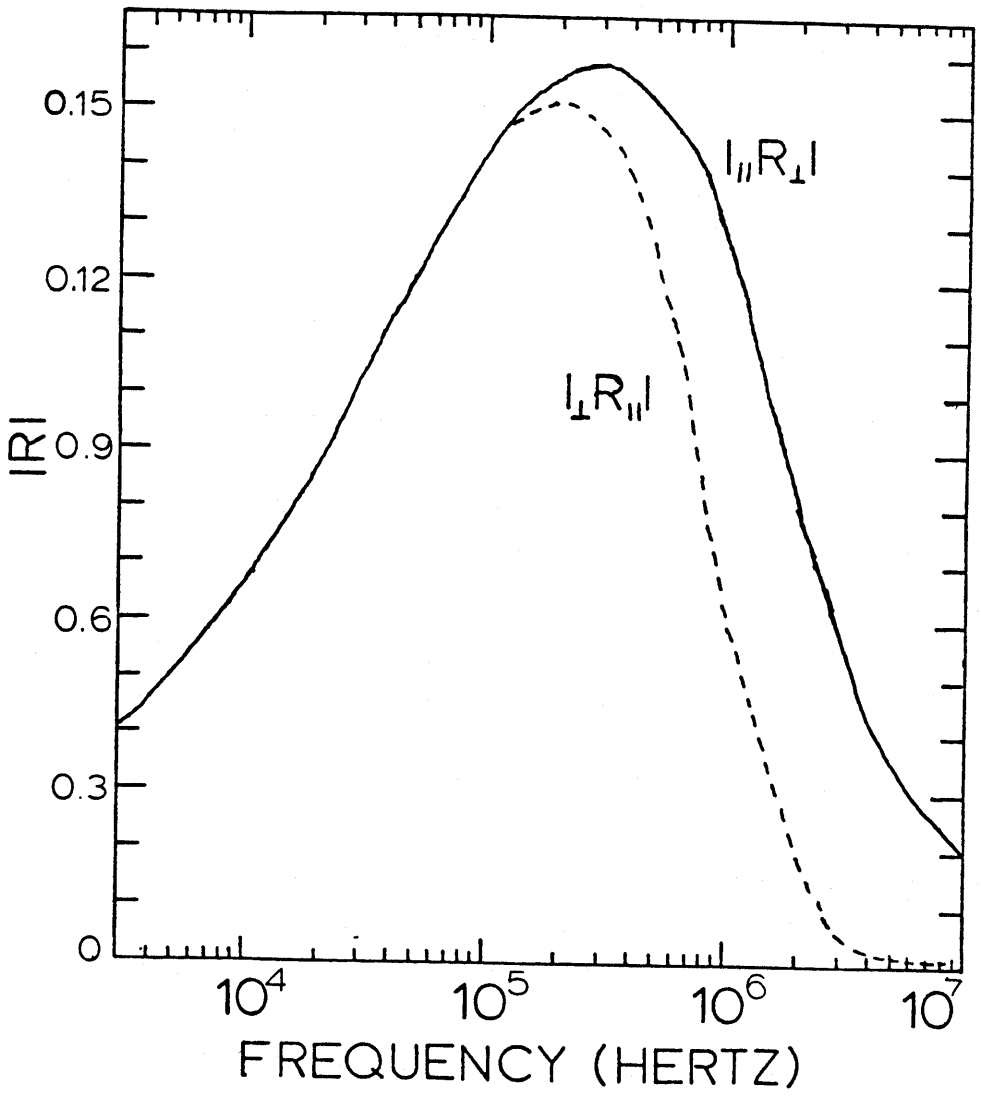

Figure 13. Cross polarization reflection coefficients for reflection from ionosphere as a function of frequency. These terms represent the degree of anisotropy.

These reflection coefficients may be used to compute the sky wave. Figure 14 shows a comparison of the perfectly conducting ionosphere reflected fields versus the ionospheric reflection coefficients calculated earlier. The fields are nearly the same up to 10^4 Hz but are attenuated severely thereafter. The observer is 215 km from a vertical dipole 1500 m high terminating on the ground with double exponential propagating up the dipole at velocity v = c. The fields are about a factor of two low since reflection from the ground at the receiver is not considered.

Figure 15 shows only E_z for the reflection from the ionosphere. Again the reflection from the ground near the receiver is not taken into account for those two figures but is considered in the complete model.

4. FREQUENCY DOMAIN RESULTS

This section is a compendium of the field calculations for sections 2 and 5. Specifically, perfectly conducting ground results refer to fields calculated by Equation 10. The ground wave fields are those calculated using Equations 46 and 51. Total fields are those calculated as a sum of the ground wave and sky wave fields. Generally $|\tilde{E}_z|$ is the output field since it dominates any measured response. The ground, when treated as an imperfect conductor, is modeled as a homogeneous half space with $\sigma = 5. \times 10^{-3}$ mho/m, permittivity $\varepsilon = 10\ \varepsilon_0$, and permeability $\mu = \mu_0$. For the ionosphere the collision frequency is $\nu = 10^6$/s, and the earth's magnetic field is $B = 5 \times 10^{-5}$ Wb/m^2. The corresponding conductivity is on the order of $\sigma = 10^{-5}$ mho/m. The first spectrum is in Figure 16. The source for this curve is a model of a return stroke which is a vertical column 1.5 km high and terminating on the ground. The column is treated as a single filament. The current pulse propagation velocity is v = c for all example curves in this section. The solid line curve represents $|\tilde{E}_z|$ in dB as function of frequency for the total field. Note that the total field

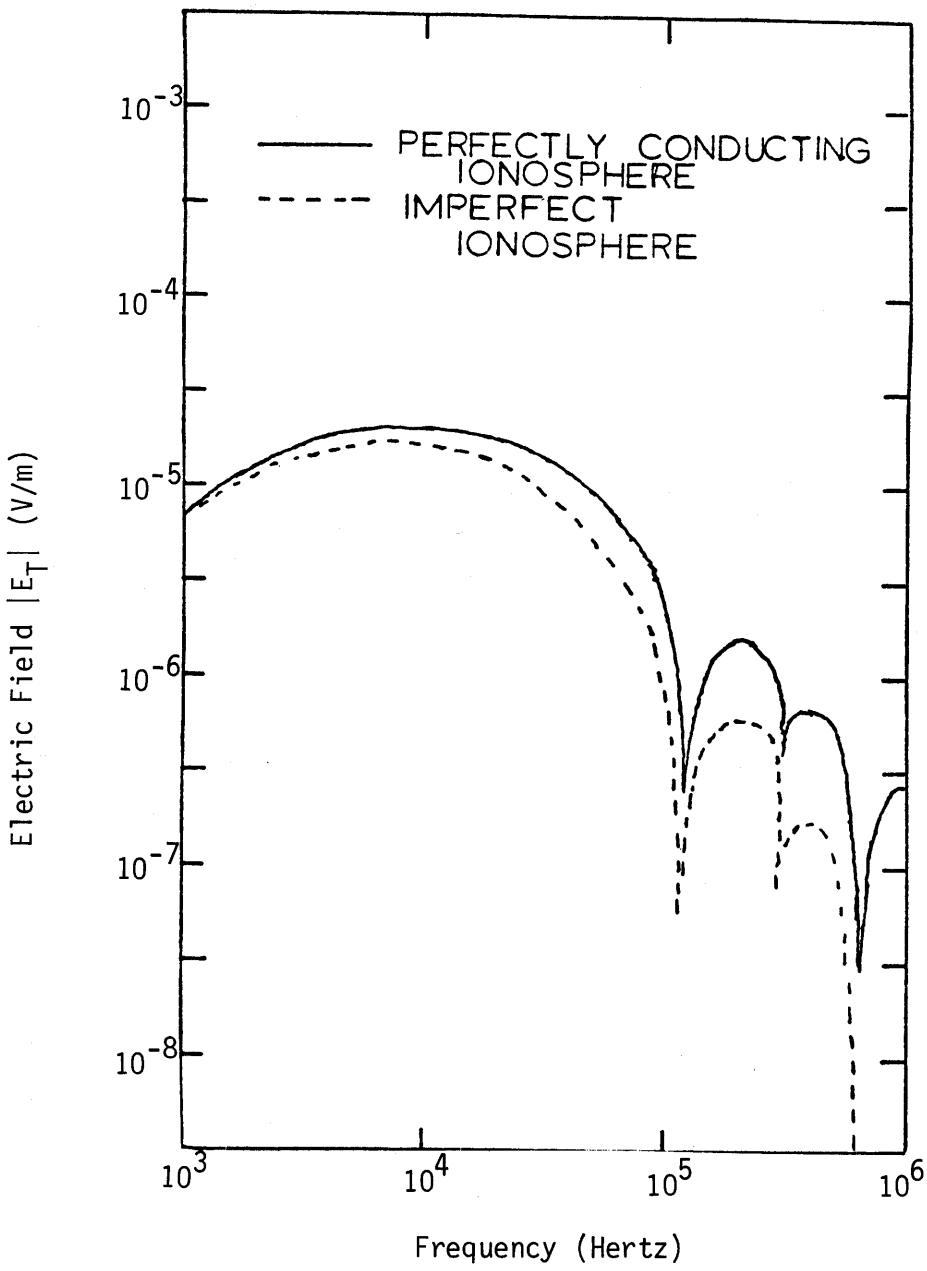

Figure 14. Total field spectrum for sky wave compared to the result for a perfectly conducting ionosphere. Return stroke model is 1.5 km vertical column.

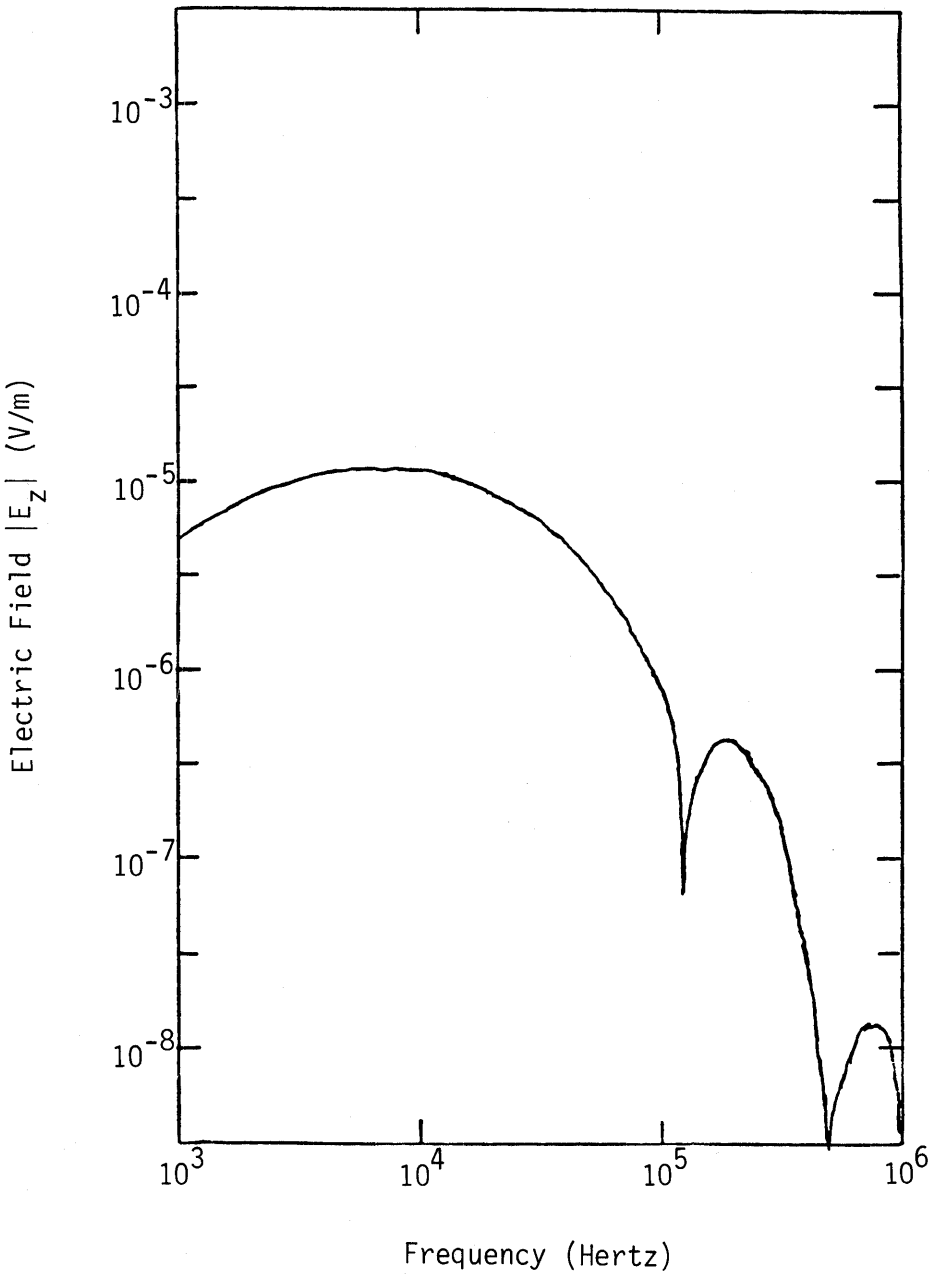

Figure 15. Vertical component spectrum of electric field. Same conditions as Figure 14 except for field component.

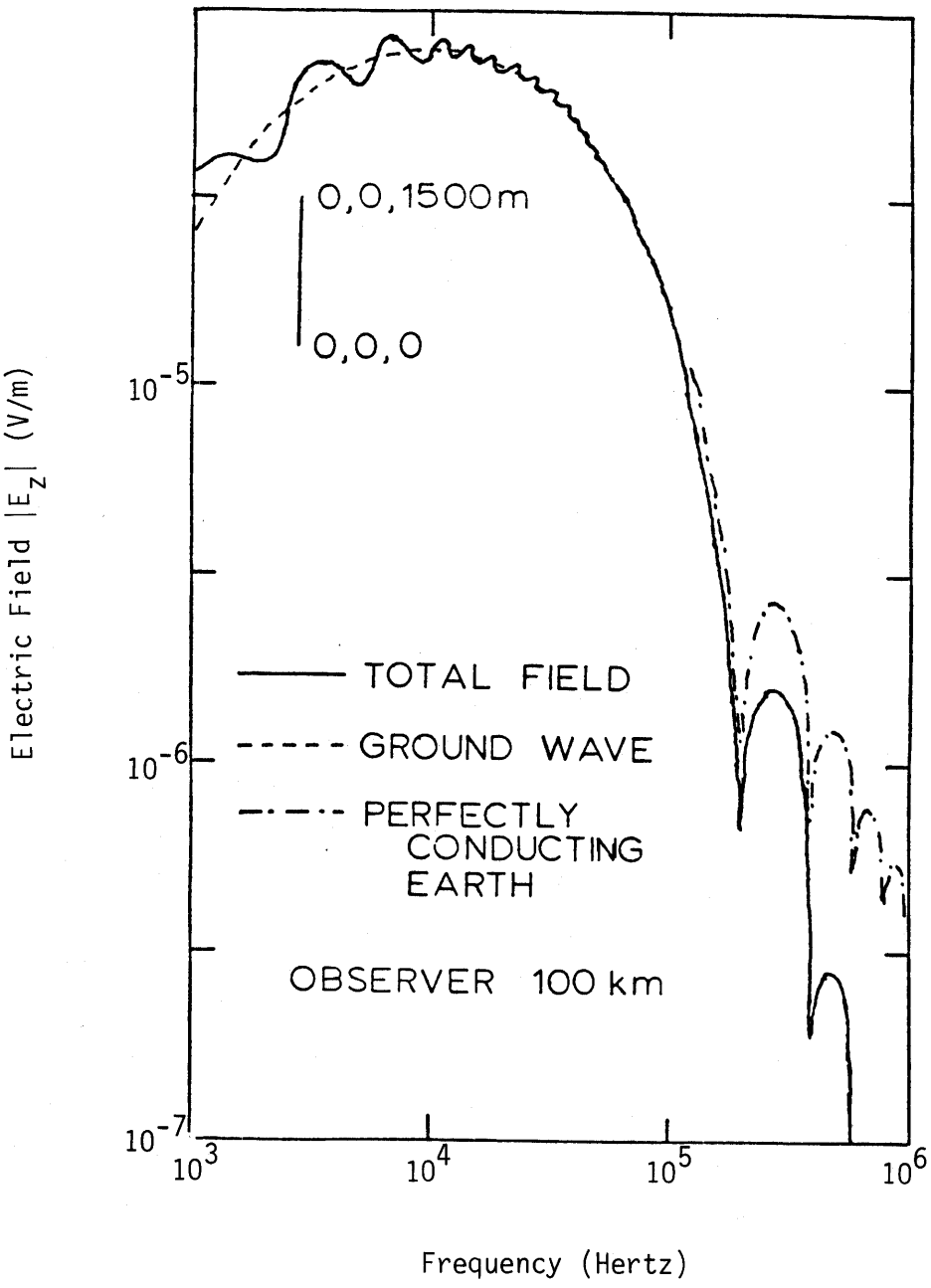

Figure 16. Electric field spectrum showing sum of sky wave and ground wave alone and the perfectly conducting ground results. Return stroke channel is modeled as a 1.5 km vertical column.

oscillates around the ground wave (dashed curve) as the sky wave destructively and constructively interferes with the ground wave. The observer is 100 km from the column. Both curves are to be compared with the perfectly conducting ground fields derived by Reference 7 denoted by alternating dots and dashes on Figure 16. Note the additional damping due to the finitely conducting earth. The point at which the curve departs from the exact solution begins earlier (linearly) with increasing observation distance. The ground wave solution agrees very well with the exact solution for low frequencies even when the condition $k_2\rho \gg 1$ is not strictly satisfied.

The analogous spectrum for a horizontal filament (corresponding to a cloud-to-cloud return stroke) is shown in Figure 17. The three curves in this graph refer to the same models as for the vertical column (Fig. 16). Note again the added attenuation due to the finite conductivity ground model. The complex structure is due again to interference with the skywave. The skywave is of the same order as the ground wave for the horizontal dipole case so the oscillations are quite large. At the high frequency end the sky wave has a set of nulls (See Fig. 13). The fields near the nulls interfere with similar fields from the ground wave creating a hash, just below 1 MHz. The horizontal line model is not very realistic since a normal cloud-to-cloud stroke would have some vertical excursion.

Finally a first order tortuous case is shown in Figure 18. The tortuous model has only three filaments as shown on the figure but demonstrates a few of the characteristics of the tortuous path. First, the initial low frequency hump decays much faster than the same hump in the single vertical segment case from Figure 16. This decay is due to the decreased apparent current pulse propagation velocity. Along each individual filament the propagation velocity remains $v = c$. The first null occurs at a lower frequency. The various filaments interfere with each other and the skywave. The vertical dipole portion dominates until the

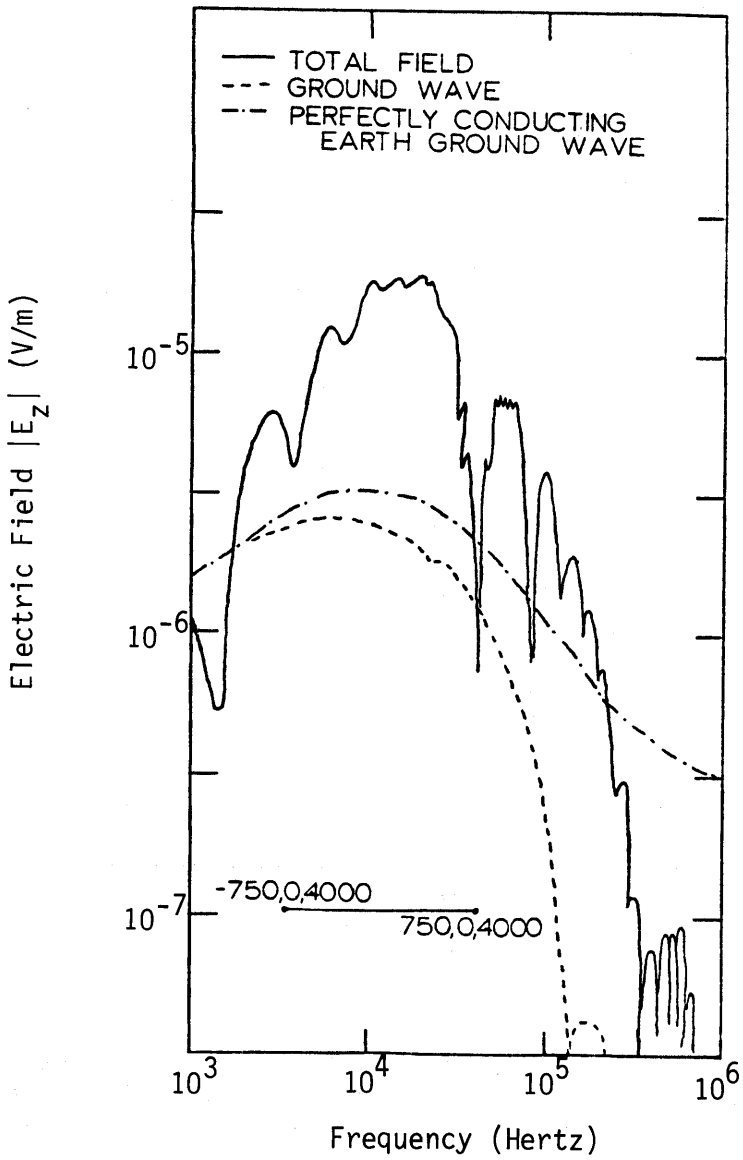

Figure 17. Electric field spectrum showing sum of sky wave and ground wave compared to ground wave alone and the perfectly conducting earth results. Return stroke channel is modeled as a 1.5 km horizontal column 4 km above the ground.

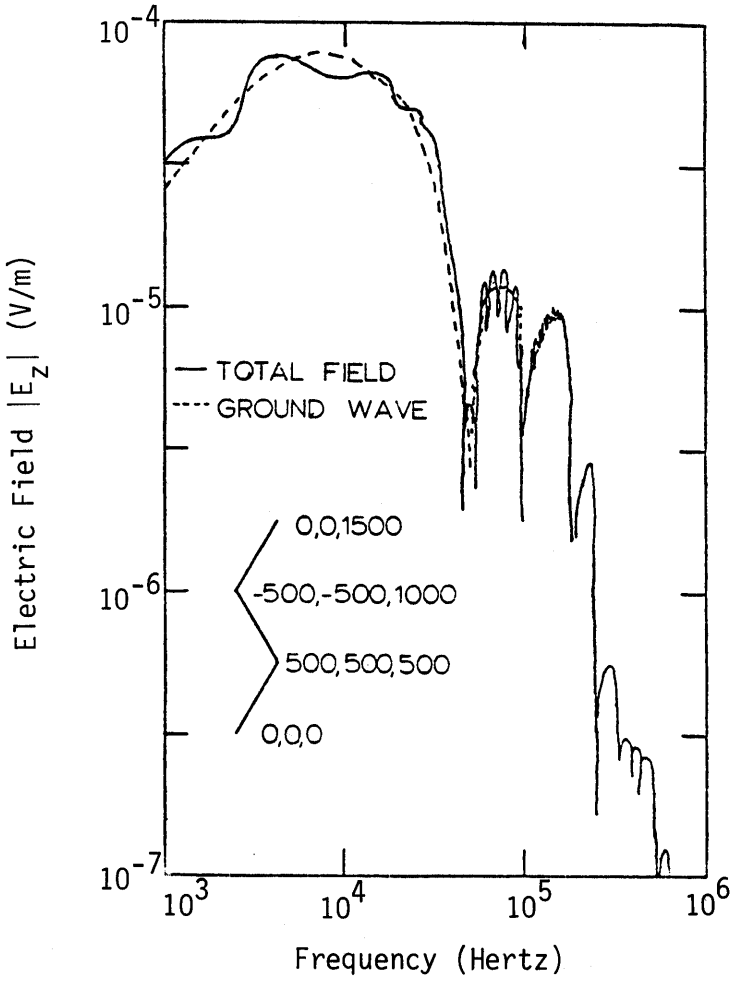

Figure 18. Electric field spectrum showing sum of sky wave and ground wave compared to ground wave alone. Return stroke channel is modeled as a tortuous channel with 1.5 km vertical extent.

horizontal component from the skywave dominates for a narrow frequency band.

5. LOW FREQUENCY RESULTS

For frequencies below about 1000 Hz the model described in Sections 2 and 3 is not really appropriate because the wavelengths involved are greater than the earth-ionospheric separation. It is now desirable to look at the propagation environment for the signals transmitted by the return stroke as a waveguide. In this method the solution is determined as a sum of waveguide modes. This approach can, in principle, be extended to all frequencies and ranges, but has some practical limitations. In the modal analysis solution the anisotropy of the ionosphere is ignored. This assumption is appropriate for frequencies below 1kHz, as can be seen from Figure 13. This solution does not contribute to the late time transient analysis since the long wavelengths would correspond to data time windows much greater than a millisecond.

The solution follows as Wait (Refs. 13, 14) for the flat earth models. The flat earth assumption restricts the applicable range to less than 250 km. The problem is treated as a three layer version of the earlier Sommerfeld half space problem.

We begin as before by assuming a Sommerfeld integral form for the scattered wave, except that the integral form must now consider scattering from above and below. For the vertical dipole case only one component is needed for the Hertz vector. The source is treated as a point dipole located at the midpoint of the channel for this case, because the return stroke channel is quite small compared to a wavelength. The expressions for the z component of the Hertz vector is, for the geometry in Figure 19

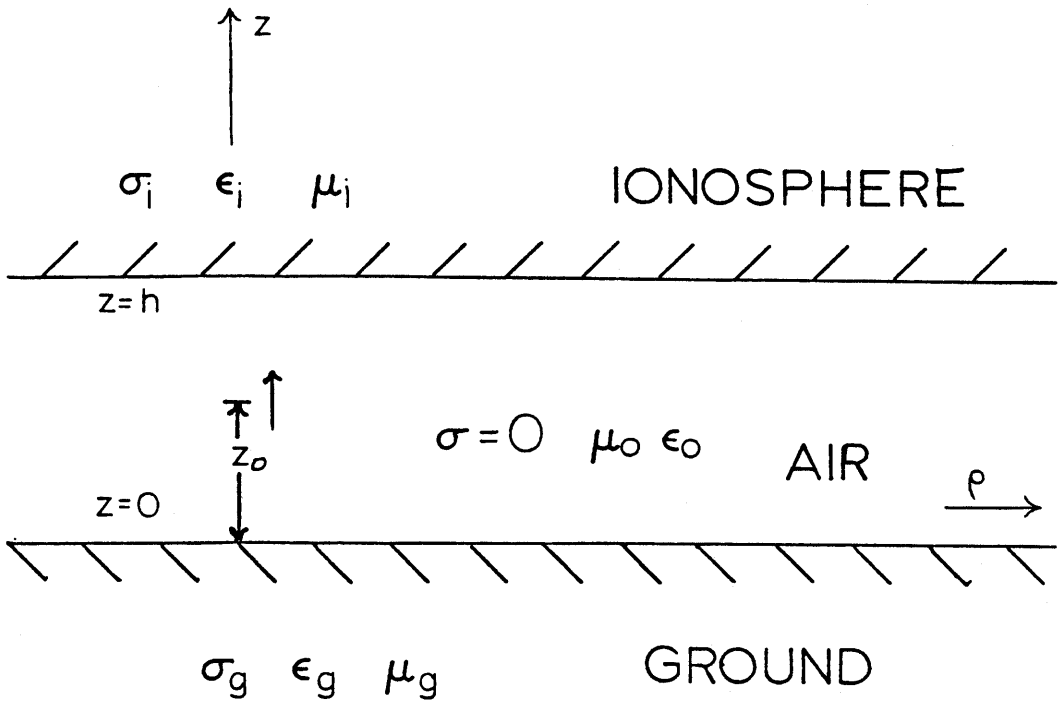

Figure 19. Geometry for waveguide model.

$$\tilde{\Pi} = \tilde{\Pi}_z^P + \int_\Gamma \left[A(C) e^{-ik_0 C z} + B(C) e^{ik_0 C z} \right] \times H_0^{(2)}(kS\rho) dC \tag{57}$$

for $0 \leq z \leq h$.

The Hertz vector for the fields transmitted into the ground is

$$\tilde{\Pi}_z^g = \int_\Gamma G(C) e^{ik_g C_g z} H_0^{(2)}(kS\rho) dC \tag{58}$$

and into the ionosphere

$$\tilde{\Pi}_z^i = \int_\Gamma I(C) e^{-k_i C_i z} H_0^{(2)}(kS\rho) dC \tag{59}$$

The notation is similar to that for Equation 23 except that a particular physical interpretation can now be established. Consider the relation

$$\lambda = k_0 \sin(\vartheta) \tag{60}$$

and if $S = \sin(\theta)$ and $C = \cos(\theta)$ in Equations 57-59 the two expressions for the Hertz vector have the same form as the integral used in Equation 23. The angle θ is physically that angle with the vertical of a ray that would be generated by an equivalent line source corresponding to the vertical dipole and the infinite number of images in the two interface planes. A ray is formed by the constructive interference of the image sources. The constructive interference forms phase fronts at various angles since the phase repeats over distances of one wavelength. (See Fig. 20.) In addition to the solutions for real angles which represent real rays in propagating modes there are also non-propagating or evanescent modes. For these

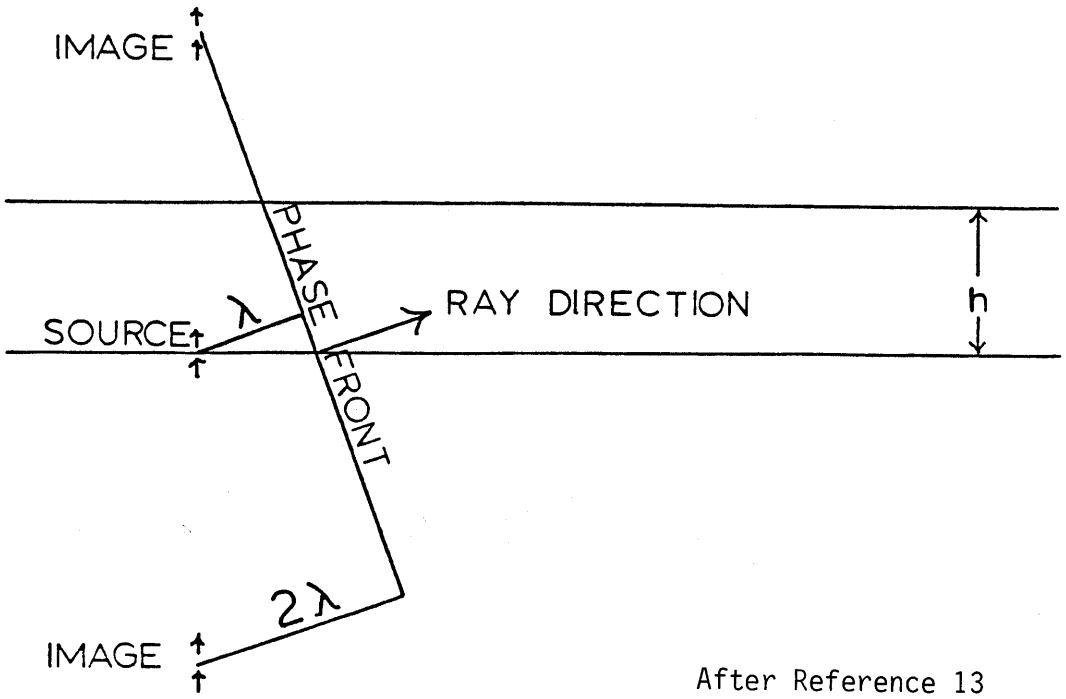

After Reference 13

Figure 20. First mode ray geometry for parallel plate model of earth-ionosphere waveguide.

modes C > 1 and are thus represented by complex angles of incidence in Equations 57-59. The integration path Γ is chosen so that the integral representation of Π_z^P is correct.

The forms in Equations 57-59 satisfy phase continuity at the boundary if

$$N_g(1 - C_g^2)^{\frac{1}{2}} = (1 - C^2)^{\frac{1}{2}} = N_i(1 - C_i^2)^{\frac{1}{2}}$$

which is just Snell's Law. The indices of refraction are

$$N_g = \left[\frac{\sigma_g + i\omega\varepsilon_g}{i\omega\varepsilon_0}\right]^{\frac{1}{2}}$$

and

$$N_i = \left[\frac{\sigma_i + i\omega\varepsilon_i}{i\omega\varepsilon_0}\right]^{\frac{1}{2}}$$

The g suffix refers to ground components, i to those for the ionosphere and o to those of free space, or the air between the boundaries.

The direct or primary contribution to the Hertz vector is

$$\tilde{\Pi}_z^P = M\frac{e^{-ik_0\left[\rho^2 + (z - z_0)^2\right]^{\frac{1}{2}}}}{\left[\rho^2 + (z - z_0)^2\right]^{\frac{1}{2}}}$$

$$= \frac{Mik_0}{2}\int_\Gamma \exp\left[-ik_0C\,|z - z_0|\right]H_0^{(2)}(kS\rho)dC \qquad (61)$$

where

$$M = \frac{\tilde{f}(\omega)L_z}{4\pi i\omega\varepsilon_0}$$

The contour Γ then extends from $-\infty$ along the negative real axis along the positive real axis to $+\infty$. The contribution for values of $C > 1$ are clearly required.

The coefficients of Equations 57-59 are chosen by requiring $k^2\tilde{\Pi}_z$ and $\partial\tilde{\Pi}_z/\partial z$ to be continuous across the two interfaces. The resulting Hertz vector for the fields between the interfaces is (Ref. 13)

$$\tilde{\Pi}_z = \frac{ikM}{2}\int_\Gamma F(C)H_0^{(2)}(kS\rho)dC \tag{62}$$

where

$$F(C) = \frac{(e^{ik_0Cz} + R_g(C)e^{-ik_0Cz})(e^{ik_0C(k-z_0)} + R_i(C)e^{-ik_0C(k-z_0)})}{e^{ik_0Ch}(1 - R_g(C)R_i(C)e^{-2ik_zCh})}$$

and

$$R_g(C) = \frac{N_gC - C_g}{N_gC + C_g}$$

$$R_i(C) = \frac{N_iC - C_i}{N_iC + C_i}$$

are the reflection coefficients for the two boundaries. With notational changes they are of the same form as Equation 28.

The integrand has poles where

$$1 - R_g(C)R_i(C)e^{-2ik_0Ch} = 0 \tag{63}$$

which is the modal equation. Exact solutions for finitely conducting earth and ionosphere are not trivial. The numerical methods of Appendix A were developed to solve this equation.

The integral may be evaluated by function theoretic means. Changing the integration variable from C to S does not result in a change of contour Γ. The contour may now be closed in the lower half plane as indicated in Figure 21. Since F(C) is odd and there is an additional C in the integrand then the integrand is even in C. Therefore crossing the branch line at S = +1 does not contribute to a change in the function and can be ignored. The resulting integral in then $-2\pi i$ times the sum of the residues plus the contribution from the indentations for $S = N_i$ and $S = N_g$. The branch line contributions are generally negligible for the case considered here. The integration for the N_i part is included in later calculations but adds little to the integration. The decaying exponential behavior of the Hankel function assures zero contribution from the two semi-circles. The solutions to the modal equation are the poles of the integral and are located as shown in Figure 21 by the x's. The waveguide modes represented by those poles along the imaginary axis are highly damped and are the evanescent contributions. Expanding the residue series results in the following expression for the Hertz vector.

$$\tilde{\Pi}_z = \frac{i\pi M}{h} \sum_{n=-\infty}^{\infty} H_0^{(2)}(k_0 S_n \rho) f_n(z_0) f_n(z) \delta_n(C) \tag{64}$$

where

$$\delta_n(C) = \left[1 + i \frac{\frac{\partial}{\partial C}\left[R_i(C) R_g(C)\right]}{2k_0 h R_i(C) R_g(C)} \right]^{-1} \Bigg|_{C = C_n}$$

The C_n are solutions to Equation 63 and

$$f_n(z) = \frac{e^{ik_0 C_n z} + R_g(C_n) e^{-ik_0 C_n z}}{2\left[R_g(C_n)\right]^{\frac{1}{2}}}$$

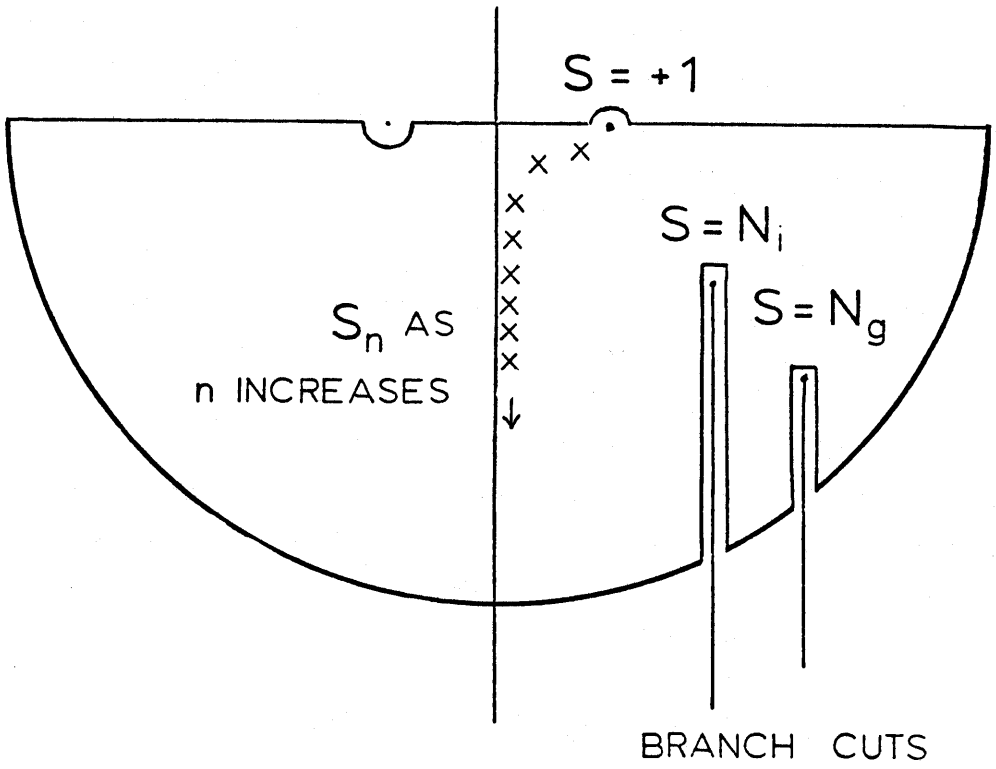

Figure 21. S-Plane showing poles (x's) and branch cuts.

When the walls are perfectly conducting (Eq. 64) reduces to

$$\tilde{\Pi}_z = \frac{ipiM}{h} \sum_{n=0,1\cdots}^{\infty} \varepsilon_n H_0^{(2)}(k_0 S_n \rho)\cos(k_0 C_n z_0)\cos(k_0 C_n z) \tag{65}$$

where the C_n are the standard parallel plate resonance solutions and $\varepsilon_0 = 1$, $\varepsilon_n = 2(n \geq 1)$.

$$C_n = \frac{n\pi}{kh} \tag{66}$$

The field solution for the vertical dipole for the dominant E_z is

$$\tilde{E}_z = \left[k_0^2 + \frac{\partial^2}{\partial z^2}\right]\tilde{\Pi}_z$$

$$= \frac{i\pi M k_0^2}{h} \sum_{n=-\infty}^{\infty} S_n^2 H_0^{(2)}(k_0 S_n \rho) f_n(z_0) f_n(z) \delta_n(C) \tag{67}$$

For the horizontal dipole, the fields may be found by finding $\tilde{\vec{\Pi}}$ in a similar way to the above, but using

$$\tilde{\vec{\Pi}} = (\Pi_x, 0, \Pi_z)$$

and boundary conditions (Eq. 48). This result is contained in Wait (Ref. 13). For this low frequency case the reflection coefficients are very near unit magnitude and so the fields $\tilde{E}_x$ and $\tilde{E}_y$ contribute very little to the fields when the observation point is near the surface. Therefore only $\tilde{E}_z$ is needed and may be obtained more simply using the reciprocity theorem (Ref. 14). A general form of the reciprocity theorem states, for no magnetic sources (Ref. 37).

$$\int\int\int \tilde{\vec{E}}^a \cdot \tilde{\vec{J}}^b \, d\tau = \int\int\int \tilde{\vec{E}}^b \cdot \tilde{\vec{J}}^a \, d\tau \tag{68}$$

Suppose $\vec{J}^b$ is chosen to be

$$\tilde{\vec{J}}^b = I_0 \delta(\vec{r}')\hat{z}$$

and $\vec{J}^a$ is chosen to be

$$\tilde{\vec{J}}^a = I_0 \delta(\vec{r})\hat{x}$$

then $\tilde{\vec{E}}^a$ and $\tilde{\vec{E}}^b$ are the corresponding field expressions. Then, carrying out the integration

$$\tilde{E}_z^a(\vec{r}') = \tilde{E}_x^b(\vec{r}) \tag{69}$$

The interpretation of this equation is that $\tilde{E}_z$ due to an x directed dipole is the same as $\tilde{E}_x$ due to the vertical dipole of the same magnitude with source and observer coordinates interchanged. Since for the vertical dipole we have $\tilde{\Pi}_z$ and

$$\tilde{E}_x = \frac{\partial^2}{\partial x \partial z}\tilde{\Pi}_z \tag{70}$$

Therefore, for the horizontal dipole contribution

$$\tilde{E}_x = -\frac{\partial}{\partial x}\left[\frac{k_0 \tilde{f}(\omega) L_x \pi}{4\pi i \omega \varepsilon_0 h} \sum_n H_0^{(2)}(k_0 S_n \rho) \times g_n(z_0) f_n(z) \delta_n(C)\right] \tag{71}$$

where f_n and $\delta_n(C)$ are the same as before but

$$k_0 g_n(z_0) = -i\frac{\partial}{\partial z_0} f_n(z_0)$$

as in Wait (Ref. 14).

For some numerical solutions to Equation 63 it is desirable to have estimates of the roots. These estimates may be derived as follows. For the frequencies below 1000 Hz, where this modal solution is used the indices of refraction (N_i,N_g) are large and the reflection coefficients may be approximated as follows.

$$R_g(C) = \frac{N_g C - C_g}{N_g C + C_g} \approx 1 - \frac{2C_g}{N_g C}$$
$$\approx \exp(-2/N_g C)$$

and similarly for the $R_i(C)$. The resonance condition then becomes

$$kCh = \pi n + \frac{i}{C}\left[\frac{1}{N_i} + \frac{1}{N_g}\right]$$

This equation may be solved as a quadratic for C with the root taken to agree with Equation 66 in the perfectly conducting limit, (i. e., N_i, $N_g \to \infty$). The result is, Wait (Ref. 13)

$$C_n \approx \frac{1}{2}\left\{\frac{\pi n}{k_0 h} + \left[\left(\frac{\pi n}{kh}\right)^2 + \frac{4i}{kh}\left[\frac{1}{N_i} + \frac{1}{N_g}\right]\right]^{\frac{1}{2}}\right\} \qquad (72)$$

then $S_n = (1 - C_n^2)^{\frac{1}{2}}$ with the sign on the square root taken to maintain S_n in the lower right quadrant. These approximate solutions may be used as starting points for exact determination of the roots of Equation 63.

The series solutions to this three layer problem are, in principle, good for all source-observer separations and for all frequencies (as long as an isotropic ionospheric model is useful). However, the number of terms that can practically be summed is limited by both round-off errors and economics.

Consider series (Eq. 67). The $F_n(z)$ and $\delta_n(C)$ are functions of order 1 and vary slowly with n. The S_n are related to solution of the modal equation. As n increases S_n increases in magnitude down the imaginary axis as in Figure 21.

The convergence of the series in Equation 67 is dominated by the behavior of the term $H_0^{(2)}(k_0 S_n \rho)$. Its eventual decay is exponential and so dominates the algebraic behavior of S_n^2, fn, and $\delta_n(C)$. Requiring $H_0^{(2)}(k_0 S_n \rho)$ to behave as a strongly decaying exponential for all terms left out of the series, places two requirements on the argument of the Hankel function.

The first is that the $S_n = (1 - C_n^2)^{\frac{1}{2}}$ can be approximated be a large negative imaginary number. Physically this requirement is to sum all propagating modes and the first few evanescent modes. The approximation

$$S_n = -\frac{in\pi}{kh} \tag{73}$$

is a reasonable substitution for S_n for the purposes of examining the convergence of Equation 67. The small variations from the strict imaginary axis or along the imaginary axis do not affect convergence, only the value of the sum. The approximation (Eq. 73) requires the restriction $Re(C_n) \gg 1$. If C_n is approximated by

$$C_n \approx \frac{n\pi}{kh} \gg 1$$

then for a given truncation index N there is a restirction on k_0.

In addition, for Equation 67 to converge the argument of the Hankel function must be large, or $kS_{N\rho} \gg 1$. This restriction places a limit on the magnitude of the radial separation distance between source and observer.

For example, assume that 10 is sufficiently larger than 1 for the convergence ratios desired and that N = 100 is the maximum number of terms that can be economically and accurately calculated, then

$$\frac{N\pi}{kh} = 10 \rightarrow \frac{nc}{2fh} = 10 \qquad (74)$$

or that $f \leq 15$ kHz is the restriction on the frequency necessitated by summing all propagating modes plus a few evanescent modes.

For the other restriction

$$kS_N\rho = 10 \rightarrow \frac{n\pi\rho}{h} = 10 \quad (h = 100km)$$

$$\rightarrow \rho \geq \frac{10h}{n\pi} = 3km$$

For other selections of N, ρ_{max} scales as 1/N, and f_{max} scales as N. For accurately located modes (as in Appendix A), N = 10 would probably be the economic upper limit for N. For modes calculated as those near the solutions for perfectly conducting boundaries (As in e. g., Wait and Carter, (Ref. 38) or in Eq. 72) then N = 1000 would be feasible.

The fields calculated for the lightning return stroke are handled as before. That is, the return stroke is assumed to be constructed of a series of interconnected filaments. Each filament is divided into a set of three orthogonal dipoles. The fields are then calculated and summed. The corrections for phase changes due to the source current propagating along the filament are irrelevant for these long wavelengths.

The waveguide solution is compared to the previously used exact solution for the perfectly conducting earth, no ionosphere, solution in Figure 22. The attenuation of the signal by the waveguide is about 6 dB over most of the frequency range. Near 1 kHz the solution meshes with the total field and ground wave solutions which are taken from Figure 16. The two mesh closely at 1 kHz in both slope and amplitude.

Figure 22 is a good example to use to summarize the features of this new model. For the first time fields may be predicted using a complex lightning current model in a realistic earth-ionosphere propagation model. The earlier models predict fields about a factor of two too high below 1000 Hertz. Above about 100 kHz the fields may be over estimated be an order of magnitude or more. Recent observations (Refs. 25, 26) indicate field behavior with rise times as fast as 30 ns. This fast behavior is successfully masked by ground wave attenuation for distances larger than a few tens of kilometers. Therefore, understanding the effect of propagation on these fields is vital if one is to use field measurements to understand lightning currents.*

6. INTEGRAL TRANSFORMS AND THE TIME DOMAIN

The solution of Maxwell's equations can be simplified by use of an integral transform to eliminate the time dependence. The resulting dif-

---

*Kirder, private communication, 1980.

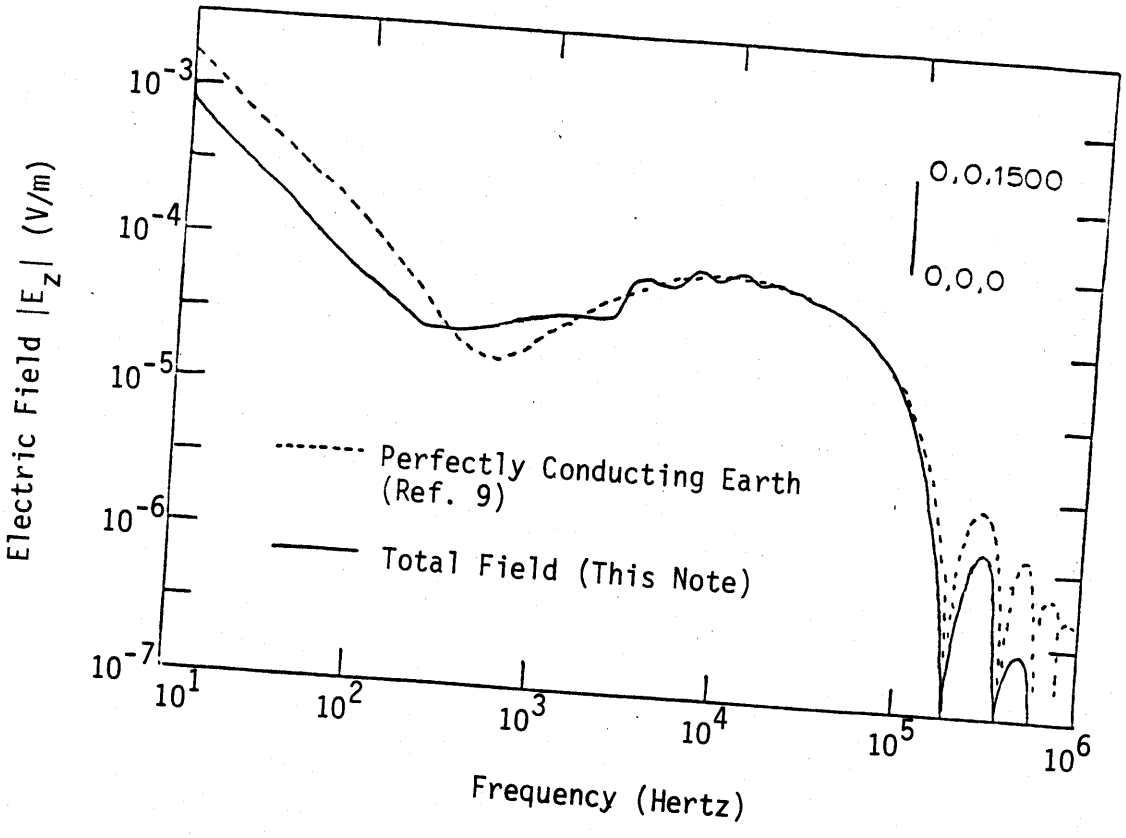

Figure 22. Electric field spectrum for full model frequency range compared to perfectly conducting earth solution. Total field includes waveguide solution below 1 kHz and total field from Figure 16 above 1 kHz.

ferential equations have one less independent variable and the time dependence may restored using the inverse transform. The most widely used transform is the Fourier transform by which one obtains the usual frequency domain solutions.

Calculation of the forward and inverse transforms, particularly for transient waveforms, and has received much attention in recent years since large computers have allowed the transform calculation. Calculation of the Fourier transform via a discrete approximation of the Fourier integral using the fast Fourier transform algorithm is a widely used technique (Ref. 39). Any discrete Fourier transform technique suffers from errors due to truncation of the integration and from errors from improper treatment of singularities of the integration axis. A way of avoiding the singularities on the integration axis and at the same time minimize the effects of the poor late time data in this problem is to use the Modified Fourier Transform (MFT) (Ref. 40). In the MFT the integration path of the inverse transform is parallel to the real frequency axis and displaced from it slightly. The MFT pair is identical to the normal Fourier transform pair for $e^{-st}f(t)$ (s real and positive) rather than for f(t) in the standard definition. Explicitly the transform pair is

$$\tilde{F}(s,\omega) = \int_{-\infty}^{\infty} e^{i\omega t}\left[e^{-st} f(t)\right] dt$$

and

$$e^{-st} f(t) = \frac{1}{2\pi}\int_{-\infty}^{\infty} e^{i\omega t}\, \tilde{F}(s,\omega) d\omega$$

where s is a constant. The FFT algorithm of Brigham (Ref. 39) is used for the explicit calculation.

An signal function $\tilde{A}(\omega)$ is particularly useful in comparing theory to data and for explicitly showing the effects of the earth-ionospheric environment on the waves propagating through the waveguide. This type of analysis, for point sources, was done for intercontinental distances by Jean, Taylor, and Wait (Ref. 41). The signal function $\tilde{A}(\omega)$ is defined by

$$\tilde{A}(\omega) = \left| \frac{\tilde{E}_z(\vec{r}_f, \omega)}{\tilde{E}_z(\vec{r}_n, \omega)} \right| \left| \frac{\vec{r}_f}{\vec{r}_n} \right| \tag{75}$$

where $\vec{r}_n$ and $\vec{r}_f$ are near and far observation points, respectively. The observation points are usually co-linear with the source. The signal function separates the 1/r geometric attenuation and explicit current effects from the field values. Remaining is the distortion of the field by the propagation path. This propagation path distortion is still dependent on the geometry of the return stroke channel and the velocity of propagation of the current pulse, so the separation of propagation effects from the source geometry is not entirely successful.

An example of comparison of data and experiment uses the modified fast Fourier transform algorithm on the MFT for both the forward and inverse transforms. Data from Lin (Ref. 42) which has a time window (150 μsec to 180 μsec) are used. The sample set of measurements for this method is a simultaneous two station set at observation points at 5.2 km and 200 km from the return stroke. The two waveforms, normalized to 100 km, are shown in Figure 23. The solid curve is the near measurement and the dashed curve is for the far measurement. The slowly varying quasi-static component in the near waveform is apparent, as well as the decreased rise time.

The signal function derived from the numerically transformed measured transient waveforms (Ref. 42) from Figure 23 are shown in Figure 24 as the solid line. The dashed line is the signal function from calculated waveforms. The near observer predicted waveform is propagated over a sea water

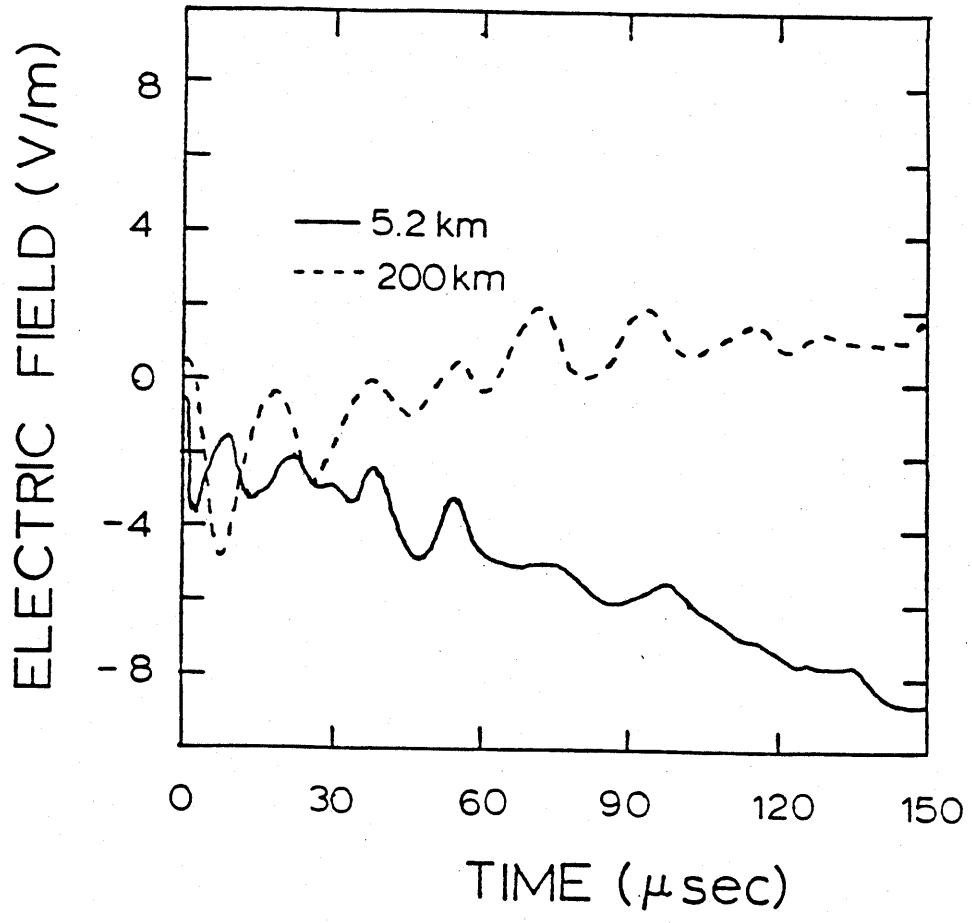

Figure 23. Simultaneous two station waveforms from a single return stroke 5.2 km and 200 km from the return stroke. Curves are digitized, normalized, and smoothed data from Reference 42.

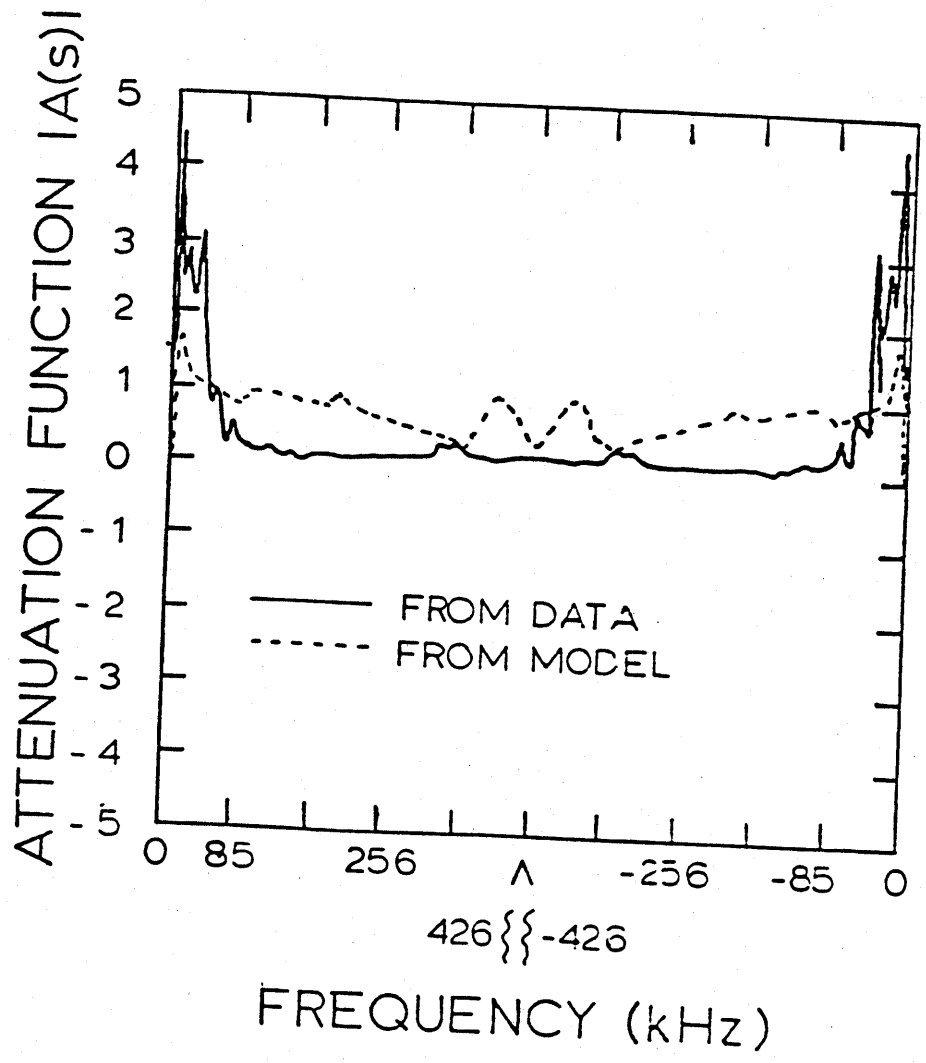

Figure 24. Signal function as a function of frequency derived from Fourier transforms of Reference 42 data and from the model of this note.

model with conductivity σ = 4 mho/m and permittivity $\varepsilon = 81\ \varepsilon_0$. The ground model for the far observer measurement is propagated entirely over a ground model with conductivity $\sigma = 2 \times 10^{-3}$ mho/m and permittivity $\varepsilon = 12\ \varepsilon_0$. The observed lightning stroke was over sea water. The transition from sea water to land which affects the waves is not considered. A predicted and observed transient waveform, is shown in Figure 25.

The $\tilde{A}(\omega)$ derived from the theoretical model, as shown in Figure 24 is multiplied by the transform of the near observation point transient waveform as shown in Figure 23. The result is inverse transformed and compared with the far observation point transient waveform in Figure 25. There is room for improvement in the agreement of the two waveforms. Better matching techniques are shown in Reference 21.

7. CONCLUSIONS

In this note the methodology of determining the effect of a finitely conducting ground and reflections from the ionosphere on a transient waveform transmitted from a lightning return stroke. In the frequency domain spectra for various transmitted electric fields are shown. The general effect of the imperfectly conducting ground is to attenuate the transmitted waveform. The added attenuation is calculated explicitly and compared to experimental data. In that comparison and in the inverse Laplace transformed results it is clear that a better specification of the environment and the return stroke current model is needed. The sensitivity of these curves to the possible parameter variations, (i. e., current pulse, velocity, variations of conductivity and permittivity with frequency and position, and filament geometry) as well as a selection of the best set of parameters for matching experimental data is shown in Reference 21 using the models of this note. The correct values of the possible parameters will be chosen from the data.

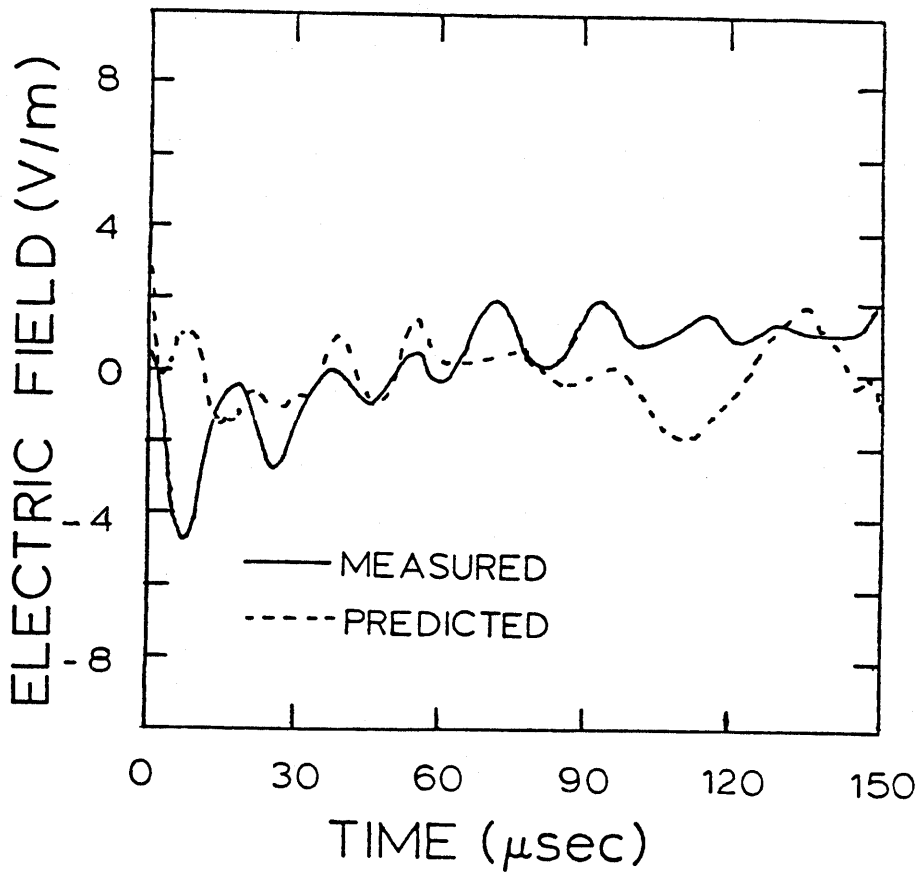

Figure 25. The 200 km transient waveform from Figure 23 compared to a predicted waveform calculated by multiplying the 5.2 km waveform of Figure 23 by the signal function calculated with this model and performing the inverse transform.

This model represents a more accurate method of predicting electric fields from lightning return strokes than has yet been available. The model successfully predicts the masking of high-frequency components of fields radiated by lightning return strokes that have only recently been discovered (Refs. 25, 26).

REFERENCES

1. Lin, Y. T., M. A. Uman, and R. B. Standler, "Lightning Return Stroke Models," J. Geophys. Res., 85, No. C3, pp. 1571-1583, 1980.

2. Uman, M. A., D. K. McLain, and E. P. Krider, "The Electromagnetic Field from a Finite Antenna," AJP, 43, pp. 33-38, 1975.

3. Uman, M. A. and D. K. McLain, "Magnetic Field of a Lightning Return Stroke," J. Geophys. Res. Res., 74, No. 28, pp. 6899-6910, 1969.

4. Uman, M. A., et al., "Correlated Electric and Magnetic Fields from Lightning Return Strokes," J. Geophys. Res., 80, pp. 373-376, 1975.

5. Smyth, J. B. and D. C. Smyth, "Lightning and its Radio Emission," Radio Science, 11, No. 12, pp. 977-984, 1976.

6. Leise, J. A. and W. L. Taylor, "A Transmission Line Model with General Velocities for Lightning," J. Geophys. Res., 82, No. 3, pp. 391-396, 1977.

7. LeVine, D. M. and R. Meneghini, Radiation from a Filament Driven by a Traveling Wave, NASA TN D-8302, 1976.

8. LeVine, D. M. and R. Meneghini, "Simulation of Radiation from Lightning Return Strokes: The Effects of Tortuosity," Goddard Space Flight Center Preprint X-953-77-154, 1977.

9. LeVine, D. M. and R. M. Meneghini, "Electromagnetic Fields Radiated from a Lightning Return Stroke: Application of an Exact Solution to Maxwell's Equations," J. Geophys. Res., 83, No. C5, pp. 2377-2384, 1978.

10. Sommerfeld, A. N., "The Propagation of Waves in Wireless Telegraphy," Ann. Phys. Series 4, 28, p. 665, 1909.

11. Banos, A., Dipole Radiation in the Presence of a Conducting Half Space, Pergamon, Oxford, 1966.

12. Galejs, J., Terrestrial Propagation of Long Electromagnetic Waves, Pergamon, Oxford, 1972.

13. Wait, J. R., Electromagnetic Waves in Stratified Media, 2nd Ed., Pergamon, Oxford, 1970.

14. Wait, J. R., "Terrestrial Propagation of Very-Low-Frequency Radio Waves, A Theoretical Investigation," J. Res. N. B. S. - D Radio Propagation, 64D, pp. 153-204, 1960.

15. Wait, J. R., "Transient Fields of a Vertical Dipole Over a Homogeneous Curved Ground," Can. J. Phys., 34, No. 1, pp. 27-35, 1956.

16. Wait, J. R., "On the Waveform of a Radio Atmospheric at Short Ranges," Proc, IRE, 44, No. 8, p. 1052, 1956.

17. Wait, J. R., "A Note on the Propagation of Electromagnetic Pulses Over the Earth's Surface," Can. J. Phys., 40, pp. 1264-1269, pp. 985-990, 1962.

18. Uman, M. A., Lightning, McGraw-Hill, New York, 1969.

19. Uman, M. A., "The Diameter of Lightning," J. Geophys. Res., 69, pp. 583-585, 1964.

20. Stratton, J. A., Electromagnetic Theory, McGraw-Hill, New York, 1941. Strawe, D. F., "Non-Linear Modeling of Lightning Return Strokes," in FAA-FTT Workshop on Ground and Lightning Technology, Melbourne, FL, pp. 9-15, 1979.

21. Gardner, R. L., Effects of Channel Model Characteristics on the Propagation of Lightning Radiated Electromagnetic Fields, Lightning Phenomenology Notes, Note 6, Air Force Weapons Laboratory, Kirtland Air Force Base, NM, 1982.

22. Golde, R. H., "Lightning Currents and Related Parameters" in Lightning, Vol. I, Physics of Lightning, R. H. Golde, ed., Academic Press, London, 1977.

23. Master, M. J., et al., "Calculation of Lightning Return Stroke Electric and Magnetic Fields Above Ground," J. Geophys. Res., 86, No. C12, 20 December 1981.

24. Haddad, H. A., Transient Electromagnetic Propagation over Conducting Earth, Ph.D. Thesis, University of Colorado, Chapter 3, 1979.

25. Baum, C. E., et al., "Measurement of Electromagnetic Properties of Lightning with 10 Nanosecond Resolution," Lightning Technology, NASA Conference Publication 2128, FAA-RD-80-30, NASA Langley Research Center, Hampton, VA.

26. Weidman, C. D. and E. P. Krider, "Submicrosecond Risetimes in Lightning Return Stroke Fields," in Lightning Technology, NASA Conference Publication 2128, FAA-RD-80-30, NASA Langley Research Center, Hampton, VA, 1980.

27. Hill, R. D. and P. J. Redmond, Comments on "Lightning and Its Radio Emission," Radio Science, 12, No. 6, pp. 731-732, 1977.

28. Pierce, E. T., "Atmospherics and Radio Noise," in Lightning, Vol. I, Physics of Lightning, R. H. Golde, ed., Academic Press, London, 1977.

29. Wait, J. R., Wave Propgation Theory, Pergamon, Oxford, 1982.

30. Booker, H. G., "The Elements of Wave Propagation Using the Impedance Concept," J. IEEE, 94, Pt. III, No. 29, pp. 171-204, 1948.

31. Bender, C. M. and S. A. Orzag, Advanced Mathematical Methods for Scientists and Engineers, McGraw-Hill, New York, 1978.

32. Wait, J. R., "Introduction to the Theory of VLF Propagation," Proc. IRE, 50, pp. 1624-1647, 1962.

33. Wait, J. R. and A. Murphy, "Multiple Reflections Between the Earth and Ionosphere in VLF Propagation," Geofisica Pura E Applicato - Milano, 35, pp. 61-72, 1956.

34. Jean, A. G., L. J. Lange, and J. R. Wait, "Ionospheric Reflection Coefficients from Sferics Measurements," Geofisica Pura E Applicata - Milano, 38, pp. 147-153, 1957.

35. Wait, J. R. and L. C. Walters, "Reflection of VLF Radio Waves from an Inhomogeneous Ionosphere, Part I, Exponentially Varying Isotropic Model," J. Res. NBS, 67D (Radio Prop.), No. 5, pp. 509-523, 1963.

36. Wait, J. R., "Recent Theoretical Advances in the Terrestrial Propagation of VLF Electromagnetic Waves," in Advances in Electronic and Electron Physics, ed. L. Marton, 25, pp. 145-209, Academic Press, New York, 1968.

37. Harrington, R. F., Time Harmonic Electromagnetic Fields, McGraw-Hill, New York, 1961.

38. Wait, J. R. and N. F. Carter, "Field Strength Calculations for ELF Radio Waves," NBS Tech Note 52, 1962.

39. Brigham, E. O., The Fast Fourier Transform, Prentice-Hall, Englewood Cliffs, NJ, 1974.

40. Day, S. J., N. Mullineux, and J. R. Reed, "Transient Response Using Fourier Transforms, Part II: Use of the Modified Fourier Transform," Int. J. Elect. Engrn. Educ., 4, pp. 31-40, 1966.

41. Jean, A. G., W. L. Taylor, and J. R. Wait, "VLF Phase Characteristics Deduced from Atmospheric Wave Forms," J. Geophys. Res., 65, pp. 907-912, 1960.

42. Lin, Y. T., Lightning Return Stroke Models, Ph.D. Thesis, University of Florida, 1978.

APPENDIX A
FLAT EARTH RESONANCES CALCULATION

Calculation of the resonant frequencies of the earth-ionospheric waveguide as used in this note requires solving the following equation for the cosine C of the complex angle of incidence.

$$R_g(C)R_i(C)e^{-2ikhC} - e^{-2in\pi} = 0 \qquad \text{(A1)}$$

The air reflection coefficients for vertical polarization for the air-ground and air-ionosphere interfaces are R_g and R_i. A similar equation must be solved for the horizontally polarized modes. The solution technique is the same as for the vertical polarization. One method of solution is to estimate the solutions C and use a Newton's (or higher order) method root finder to calculate a better estimate for the root. For low frequencies this method works well. Below about 2500 Hz the reflection coefficients are only slightly different from the perfectly reflecting case (e.g., $R_i = R_g = 1$). The solutions of Equation A1 are the well approximated by the parallel plate waveguide solutions.

$$C_n = \frac{n\pi}{kh} \qquad \text{(A2)}$$

To solve Equation A1 more precisely the following method may be used. Suppose we are solving

$$Z(z) = X(x,y) + iY(x,y) = 0 \qquad \text{(A3)}$$

where $z = x + iy$, and X and Y are the real and imaginary part of z. If we have an approximation to the zero of A(z), say $z_n = s_n + iy_n$ then a better approximation, z_{n+1}, is given by the solutions of

$$x_{n+1}\frac{\partial X}{\partial x}|_{x=x_n} + y_{n+1}\frac{\partial X}{\partial y}|_{y=y_n} = -X(x_n,y_n) + x_n\frac{\partial X}{\partial x}|_{x=x_n} + y_n\frac{\partial X}{\partial y}|_{y=y_n}$$

$$x_{n+1}\frac{\partial Y}{\partial x}|_{x=x_n} + Y_{n+1}\frac{\partial Y}{\partial y}|_{y=y_n} = -Y(x_n,y_n) + x_n\frac{\partial Y}{\partial x}|_{x=x_n}$$

$$+ y_n\frac{\partial y}{\partial Y}|_{y=y_n} \qquad \text{(A4)}$$

The derivatives may be calculated by the approximation given in the following example

$$\frac{\partial X(x,y)}{\partial x} = \frac{X(x + g(x),y) - X(x,y)}{g(x)} \qquad \text{(A5)}$$

The formula (Eq. A5) is exact in the limit g(x) → 0. If g(x) is set to a small constant this technique is the familiar secant method. The zero is approached more rapidly at the expense of some instability far from the zero if g(x) is set to =X(x,y) (Ref. A1). This method is known as Steffenson's method. The algorithm is second order in the sense that the error term is proportional to the second order term in a Taylor expansion.

At higher frequencies R_g remains near $R_g = 1$ but R_i becomes small and $R_i = -1$ yields a better starting point. In the limit as $R_i \to -1$ the C_n are given by

$$\overline{C}_n = \pi(n - \frac{1}{2})/kh \qquad \text{(A5)}$$

A better approximation for higher frequencies is given by (Ref. A2)

$$C_n \approx \frac{\pi(n-1/2) + i/(N_g\overline{C})}{kh - iN_i^2[N_i^2-1 + (\overline{C}_n)^2]^{-1/2}} \qquad \text{(A6)}$$

The approximation (Eq. A6) coupled with the iteration method above determines the zeroes efficiently up to about f = 30 kHz. Above this frequency the approximations from (Eq. A6) drift into the second quadrant and so are not correct. The trajectory of C, as given by (Eq. A6) as a function of frequency is shown in Figure A1 as compared to the numerically computer result. The approximation does not match the curl-up of the numerical result for frequencies above 30 kHz.

The desired zero is still known to lie within a region in the complex plane bounded by $(n - 1)\pi/kh$ and $n\pi/kh$ on the real axis and by 0 and a small constant on the imaginary axis. The zero may be determined from a contour integration around that contour (Ref. A3).

$$\frac{1}{2\pi i}\int_c z^N f'(z)/f(z) = \sum_{i=1}^{M} z_i^N - \sum_{j=1}^{K} w_j^N \qquad \text{(A7)}$$

The z_i are the zeroes of f(z) within the contour C and the w_j are the poles. The function defined in (Eq. A1) is analytic in this contour so the second sum disappears. For N = 0 (Eq. A7) determines the number of zeroes so that possibility of the contour encircling two zeroes can be checked. For the cases here the above contour encloses only one zero and that zero is given by (Eq. A7) for N = 1. For the calculations for Ref. A4 above f = 30 kHz the root was estimated by (Eq. A7) using an 8 point gaussian quadrature for each root. The code used was a modified version of the Code SEARCH (Ref. A5). If the iteration method did not converge 20 point quadrature was used to determine the zero.

The numerical integration technique has the advantage of required only one particular number of function evaluations per root (usually ≈ 32). The search type routines (i.e., Newton's method or contour following) require 3 evaluations per iteration. There is a trade-off.

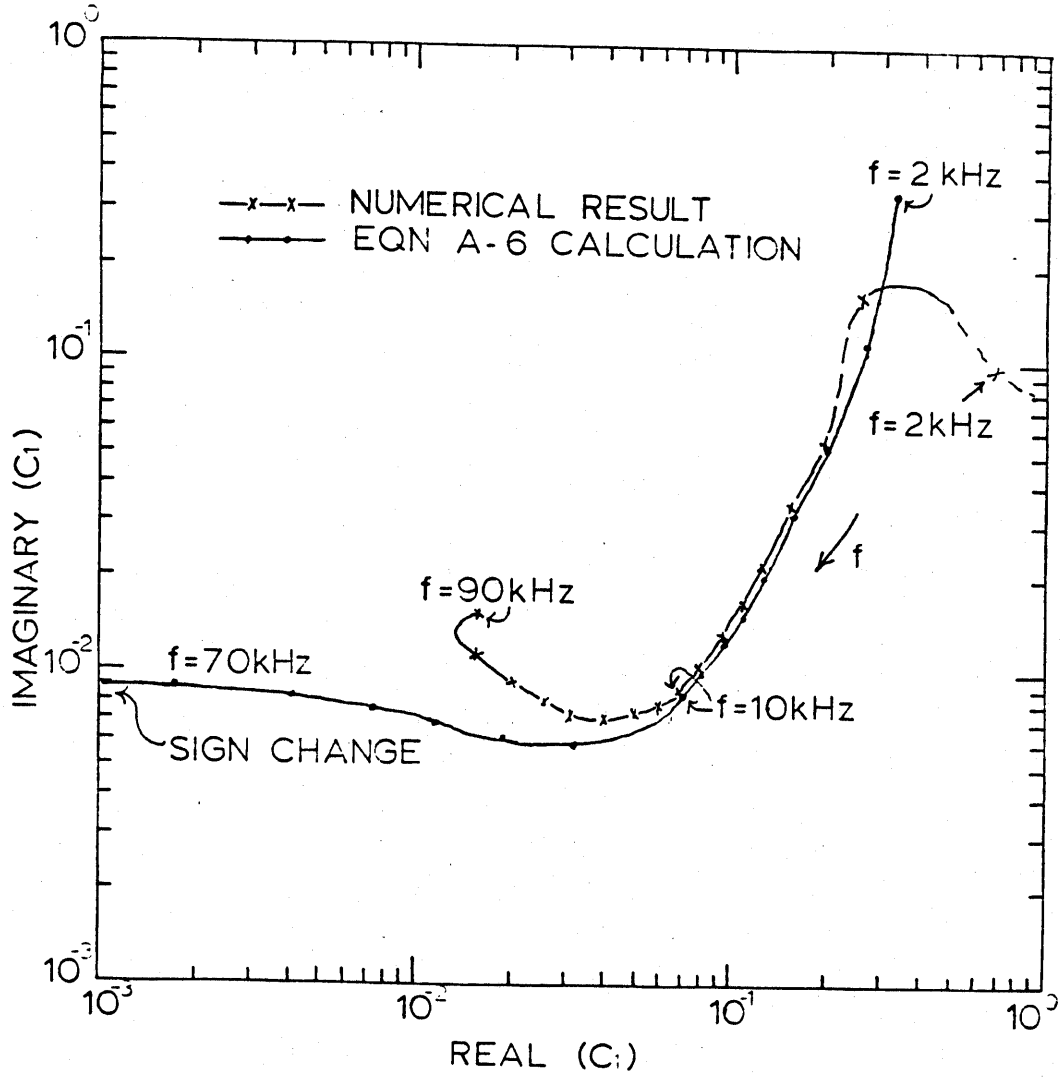

Figure A1. Trajectories of $C_1(f)$ as computed by approximation (Eq. A6) compared to numerical solution of Equation A1.

REFERENCES

A1. Dahlquist, G. and A. Bjorck, Numerical Methods, Prentice Hall, Englewood Cliffs, NJ, 1974.

A2. Wait, J. R., Electromagnetic Waves in Stratified Media, 2nd Ed., Pergamon, Oxford, 1970.

A3. Smirnov, V. I., A Course in Higher Mathematics, Vol. II, Part Two, Pergamon, Oxford, 1964.

A4. Gardner, R. L., Effects of Channel Model Characteristics on the Propagation of Lightning Radiated Electromagnetic Fields, Lightning Phenomenology Notes, Note 6, Air Force Weapons Laboratory, Kirtland Air Force Base, NM, 1982.

A5. Singaraju, B. K., D. V. Giri, and C. E. Baum, Further Development in the Application of Contour Integration to the Evaluation of Zeroes of Analytic Functions and Relevant Computer Programs, EMP Note Series, Mathematics Note 42, C. E. Baum, ed., Kirtland AFB, NM, 1976.

APPENDIX B
CALCULATION OF F(p)

Values for the attenuation function, F(p), as defined in Equation 40 are frequently needed in a study of the type performed in this note. Correct evaluation of the function is not entirely straight forward. Explicitly F(p) is written as

$$F(p) = 1 - i(\pi p)^{\frac{1}{2}} e^{-p} erfc(ip^{\frac{1}{2}}) \tag{B1}$$

The argument p is nearly real. Values of the complementary error function for complex argument may be calculated by using the series (Ref. B1)

$$erfc(x + iy) = erfc(x) - \frac{e^{-x^2}}{2\pi x}[(1 - \cos(2xy)) + i\sin(2xy)]$$

$$- \frac{2}{\pi} e^{-x^2} \sum_{n=1}^{\infty} \frac{e^{\frac{-1}{4n^2}}}{n^2 + 4\pi^2}[f_n(x,y) + ig_n(x,y)] \tag{B2}$$

where

$$f_n(x,y) = 2x - 2x\cosh(ny)\cos(2xy) + n\sinh(ny)\sin(2xy)$$

and

$$g_n(x,y) = 2x\cosh(ny)\sin(2xy) + n\sinh(ny)\cos(2xy)$$

Care must be taken to evaluate all arguments of exponentials (including hyperbolics) together to eliminate truncation errors. The real argument part of (Eq. B2) may be evaluated over part of the required values using the rational approximation

$$erfc(x) = (a_1 t + a_2 t^2 + a_3 t^3 + a_4 t^4 + a_5 t^5) e^{-x^2} + \varepsilon(x) \qquad (B3)$$

where

$$t = \frac{1}{1 + qx} \quad , \quad |\varepsilon(x)| \leq 1.5x\,10^{-7}$$

and

$q = 0.3275911$

$\alpha_1 = 0.259829592$

$\alpha_2 = -0.284496736$

$\alpha_3 = 1.421413741$

$\alpha_4 = -1.453152027$

$\alpha_5 = 1.061405429$

Equation B3 is quite accurate but does undergo a sign change at certain large values. To avoid this direct numerical integration is used.

For large values of $|p|$ the asymptotic expansion is most efficient. The asymptotic expansion used here is

$$F(p) = \sum_{m=1}^{\infty} (-1)^m \frac{1.3....(2m-1)}{(-2p)^m} \qquad (B4)$$

For this study for $|p| < 0.11$, Equation B2 was used for $erfc(ip^{\frac{1}{2}})$ and (Eq. B1) evaluated directly. For $0.11 < |p| < 5$, (p) was evaluated numerically with the exponential in F(p) taken into the integral. Finally for $|p| > 5$, (Eq. B4) was used.

REFERENCES

B1. Abramowitz, M. and I. A. Stegun, Handbook of Mathematical Functions, Dover, New York, 1968.

☆U.S. GOVERNMENT PRINTING OFFICE: 1983 — 676-142/115